Title

Parallel CRISPR-Cas9 screens identify mechanisms of PLIN2 and lipid droplet regulation.

Journal

Developmental Cell, 58(18)

Authors

Roberts, Melissa

Deol, Kirandeep

Mathiowetz, Alyssa

et al.

Publication Date

2023-09-25

DOI

10.1016/j.devcel.2023.07.001

Peer reviewed

HHS Public Access

Author manuscript

Dev Cell. Author manuscript; available in PMC 2024 September 25.

Published in final edited form as:

Dev Cell. 2023 September 25; 58(18): 1782–1800.e10. doi:10.1016/j.devcel.2023.07.001.

Parallel CRISPR-Cas9 screens identify mechanisms of PLIN2 and lipid droplet regulation

Melissa A. Roberts[1,2], **Kirandeep K. Deol**[1,2], **Alyssa J. Mathiowetz**[1,2], **Mike Lange**[1,2], **Dara E. Leto**[3], **Julian Stevenson**[2], **Sayed Hadi Hashemi**[4], **David W. Morgens**[5], **Emilee Easter**[1,2], **Kartoosh Heydari**[6], **Mike A. Nalls**[7,8,9], **Michael C. Bassik**[10], **Martin Kampmann**[11,12], **Ron R. Kopito**[3], **Faraz Faghri**[7], **James A. Olzmann**[1,2,11,13,*]

[1]Department of Molecular and Cell Biology, University of California, Berkeley, Berkeley, CA 94720, USA.

[2]Department of Nutritional Sciences and Toxicology, University of California, Berkeley, Berkeley, CA 94720, USA.

[3]Department of Biology, Stanford University, Stanford, CA 94305, USA.

[4]Department of Computer Science, University of Illinois at Urbana-Champaign, Urbana, IL 61820, USA.

[5]Department of Plant and Microbial Biology, University of California, Berkeley, Berkeley, CA 94720, USA.

[6]Cancer Research Laboratory FACS Core Facility, University of California, Berkeley, CA 94720, USA

[7]Data Tecnica International, LLC, Washington, DC, USA.

[*]Correspondence: olzmann@berkeley.

AUTHOR CONTRIBUTIONS

M.A.R. and J.A.O. conceived of the project, designed the experiments, and wrote the manuscript. All authors read, edited, and contributed to the manuscript. J.S. and K.K.D. contributed to the generation of reporter cell lines. M.A.R., K.K.D., and A.J.M. performed the genetic screens with assistance from D.E.L., D.W.M, and M.C.B. CRISPRlipid was built together with M.A.N., F.F., S.H.H., A.J.M., and M.K. M.L. performed and analyzed the lipidomics experiments. K.H. assisted with FACS and E.E. assisted in the validation of candidate regulators. We are grateful to Drs. Kivanc Birsoy (Rockefeller University), Suzanne Pfeffer (Stanford University), Albert Lu (University of Barcelona), Taroh Kinoshita and Yicheng Wang (Osaka University), and Tony Wyss-Coray (Stanford University) for contributing their published functional genomics data sets to CRISPRlipid. We thank Dr. Zhipeng Li for helpful discussions and critical reading of the manuscript. We thank Doug Guastaferro and Naveed Ziari for technical assistance with casTLE analysis.

DECLARATION OF INTERESTS

J.A.O. is a member of the scientific advisory board for Vicinitas Therapeutics and has patent applications related to ferroptosis. M.K. is an inventor on a US patent related to CRISPRi and CRISPRa screening; serves on the scientific advisory boards of Engine Biosciences, Casma Therapeutics, Cajal Neuroscience and Alector; and is a consultant to Modulo Bio and Recursion Therapeutics. The remaining authors declare no competing interests. F.F. and M.A.N.'s participation in this project was part of a competitive contract awarded to Data Tecnica International LLC by the National Institutes of Health to support open science research. M.A.N. also currently serves on the scientific advisory board for Clover Therapeutics and is an advisor to Neuron23 Inc. M.B. has outside interest in DEM Biopharma.

INCLUSION AND DIVERSITY

We support inclusive, diverse, and equitable conduct of research.

[8]Center for Alzheimer's and Related Dementias, National Institutes of Health, Bethesda, MD 20892, USA.

[9]Laboratory of Neurogenetics, National Institute on Aging, National Institutes of Health, Bethesda, MD 20892, USA.

[10]Department of Genetics, Stanford University, Stanford, CA 94305, USA.

[11]Chan Zuckerberg Biohub, San Francisco, CA 94158, USA.

[12]Institute for Neurodegenerative Diseases, Department of Biochemistry and Biophysics, University of California, San Francisco, San Francisco, CA 94158, USA.

[13]Lead contact

SUMMARY

Despite the key roles of perilipin-2 (PLIN2) in governing lipid droplet (LD) metabolism, the mechanisms that regulate PLIN2 levels remain incompletely understood. Here, we leverage a set of genome-edited human PLIN2 reporter cell lines in a series of CRISPR-Cas9 loss-of-function screens, identifying genetic modifiers that influence PLIN2 expression and post-translational stability under different metabolic conditions and in different cell types. These regulators include canonical genes that control lipid metabolism as well as genes involved in ubiquitination, transcription, and mitochondrial function. We further demonstrate a role for the E3 ligase MARCH6 in regulating triacylglycerol biosynthesis, thereby influencing LD abundance and PLIN2 stability. Finally, our CRISPR screens and several published screens provide the foundation for CRISPRlipid (http://crisprlipid.org), an online data commons for lipid-related functional genomics data. Our study identifies mechanisms of PLIN2 and LD regulation and provides an extensive resource for the exploration of LD biology and lipid metabolism.

Graphical Abstract

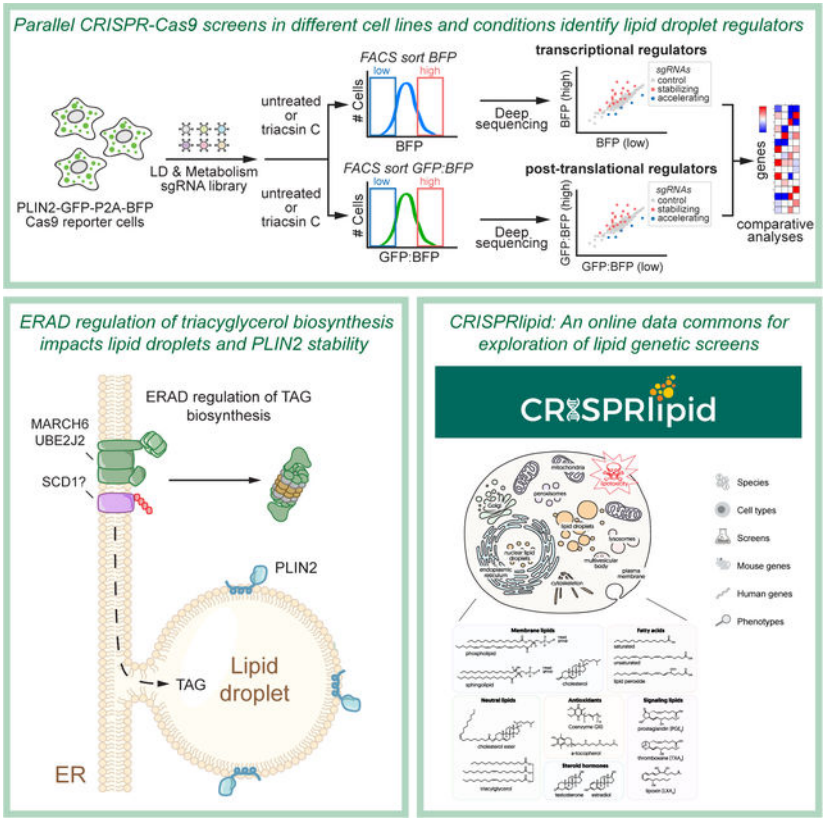

eTOC blurb

Roberts et al. perform multiple CRISPR screens in genetically-edited fluorescent PLIN2 reporter cell lines to identify regulators of PLIN2, revealing the ERAD E3 ligase MARCH6 as a regulator of triacylglycerol biosynthesis and lipid droplets. To promote exploration of lipid-related genetic screen data, they develop CRISPRlipid as an online data commons.

INTRODUCTION

Lipid droplets (LDs) are the primary cellular organelle for lipid storage[1,2]. LDs form at the endoplasmic reticulum (ER) through a stepwise process involving neutral lipid synthesis, phase separation of neutral lipids to form a lens structure within the ER bilayer, and budding of the LD from the cytosolic leaflet of the ER membrane[3,4]. These processes are catalyzed by ER proteins such as seipin, which forms an oligomeric complex that mediates triacylglycerol (TAG) aggregation to nucleate sites of LD biogenesis[3,4]. As hubs of lipid metabolism, LDs provide a dynamic lipid repository that can safely sequester lipids to prevent lipotoxicity and can be mobilized upon cellular demand to provide substrates for the generation of energy (i.e., β-oxidation) or the biosynthesis of lipid signaling molecules and membranes[1,2].

LDs consist of a core of neutral lipids, mostly TAG and cholesteryl esters, surrounded by a phospholipid monolayer. Proteins are absent from the core of LDs, and a distinctive set of LD integral and peripheral proteins (i.e., the LD proteome) associate with the surrounding

LD phospholipid monolayer and regulate LD biogenesis, breakdown, and interactions with neighboring organelles[5–8]. The perilipin proteins (PLIN1-5) are abundant LD proteins that are often referred to as LD coat proteins, and at least one PLIN family member is invariably found on LDs[9,10]. The PLIN proteins share sequence homology, including a series of 11-mer repeats that mediate LD insertion and anchoring[9,10]. PLIN2, 3, and 5 also contain a C-terminal four-helix bundle and a unique α–β domain that may bind lipids[9,10]. PLIN proteins exhibit distinct tissue distributions, and while most regulate lipolysis, the different family members have additional unique functions that include mediating LD-organelle interactions at membrane contact sites, integrating nutrient signaling cascades that influence LD dynamics, and regulating the generation of lipid signaling molecules[9,10].

PLIN2 is a ubiquitously expressed protein that regulates LDs, particularly in non-adipose tissues such as the liver. Global PLIN2 knockout (KO) mice exhibit reduced liver TAG levels and steatosis as well as resistance to diet-induced obesity[11]. Moreover, liver-specific deletion of PLIN2 reduces liver steatosis, fibrosis, and inflammation, potentially by enhancing lipoprotein secretion and fatty acid oxidation while simultaneously suppressing *de novo* lipogenesis[12,13]. These beneficial phenotypes may also be explained by PLIN2's competition with the rate-limiting enzyme in lipolysis, PNPLA2 (also known as ATGL), for LD association, which consequently inhibits lipolysis[14]. In humans, an S251P polymorphism in PLIN2 has been connected to non-alcoholic steatohepatitis (NASH) and high serum lipid levels, but also with insulin sensitivity[15–17]. In addition, overexpression of PLIN2 increases LDs in a wide variety of tissues and high levels of PLIN2 are associated with several diseases, including hepatic steatosis[18,19], conditions associated with high amounts of inflammation [20], and several forms of cancer[21]. Thus, PLIN2 and LDs exhibit a reciprocal relationship, with LDs stabilizing PLIN2 and PLIN2 stabilizing LDs[22].

The influence of PLIN2 levels on LD metabolism and the connections of PLIN2 with disease pathogenesis underscore the importance of achieving a comprehensive understanding of the mechanisms that govern PLIN2 levels. Here, we performed a series of parallel CRISPR-Cas9 loss-of-function screens in a set of genome-edited PLIN2 reporter cells. These screens provide a phenotype-rich resource detailing the genetic modifiers that regulate PLIN2 and LDs, including regulators of PLIN2 expression and protein stability. Using data from our screens together with published lipid-focused screens, we establish CRISPRlipid (http://crisprlipid.org/) as an extensible, community-driven data commons for the exploration and comparison of data from functional genomics screens related to lipid biology.

RESULTS

Generation of a genome-edited PLIN2-GFP reporter cell line

CRISPR-Cas9 genome editing was used to generate a fluorescence-based PLIN2 reporter cell line in Huh7 hepatocellular carcinoma cells (Figure 1A). In this cell line, PLIN2 is endogenously tagged with enhanced green fluorescent protein (GFP) and an S-tag at its C-terminus (PLIN2-GFP) (Figure 1A). Endogenous tagging is essential to retain the normal regulation and levels of PLIN2 expression and to avoid artifacts associated with PLIN2 overexpression, such as aberrant stabilization of LDs[14,23]. The edited PLIN2-

GFP cells were distinguishable from parental cells by their increased GFP fluorescence using flow cytometry (Figure 1B). Immunoblotting for PLIN2 revealed the presence of both endogenous, untagged PLIN2 and GFP-tagged PLIN2 (Figure 1C, *middle blot*), and immunoblotting for GFP confirmed the presence of PLIN2-GFP as well as the absence of any free GFP (Figure 1C, *top blot*). These data indicate a heterozygous insertion of GFP in frame with PLIN2. Importantly, PLIN2-GFP properly localized to the LD membrane encircling the neutral lipid core of LDs (Figure 1D).

To further characterize the PLIN2-GFP reporter cell line, we examined the effects of oleate-stimulated LD biogenesis and triacsin C treatment. Triacsin C is an acyl-CoA synthetase inhibitor that blocks TAG biosynthesis and starves cells of activated fatty acids, triggering LD breakdown. Consistent with the strong correlation between PLIN2 levels and LD abundance, endogenous PLIN2 and PLIN2-GFP levels increased following oleate treatment and decreased in response to triacsin C treatment (Figure 1E,F; Figure S1A,B). As expected, the changes in PLIN2-GFP levels correlated with the changes in the fluorescence of the neutral lipid stain monodansylpentane (MDH) (Figure S1B). To define the mechanisms that regulate PLIN2-GFP decrease during lipolysis, we introduced single guide RNAs (sgRNAs) targeting the TAG lipase *PNPLA2* (also known as ATGL) and its co-activator *ABHD5* (also known as CGI-58) into PLIN2-GFP cells expressing Cas9. Depletion of *PNPLA2* or *ABHD5* led to an increase in PLIN2-GFP levels under basal conditions and a dramatic block in the PLIN2-GFP decrease following a triacsin C treatment (Figure 1G–I; Figure S1C,D), indicating that LD degradation during triacsin C treatment requires PNPLA2 and ABHD5-dependent lipolysis. These findings highlight the differential impact of canonical LD regulatory genes depending on the metabolic state of the cell, underscoring the importance of characterizing LD regulation under different metabolic conditions.

PLIN2 is stabilized by its insertion into LDs and uninserted PLIN2 is degraded by the ubiquitin-proteasome system (UPS) in cell types that have few LDs, such as HEK293 and HeLa[24–26]. In contrast to HEK293 and HeLa cells, Huh7 cells have large amounts of PLIN2-positive LDs. Whether this pool of LD-inserted PLIN2 in Huh7 cells is degraded by the proteasome or an alternative pathway, such as via autophagy or the lysosome, during the lipolytic consumption of LDs is unknown. During triacsin C-induced LD degradation, the decrease in PLIN2-GFP levels was strongly blocked by co-incubation with the proteasome inhibitor MG132 or E1 ubiquitin-activating enzyme inhibitor MLN7243 (Figure 1J,K; Figure S1E–G). Co-incubation with leupeptin, bafilomycin A1 (baf A1), or lalistat 2, inhibitors of lysosomal functions, had no effect (Figure 1J,K; Figure S1G). These findings indicate that the clearance of LD-inserted PLIN2 during lipolysis requires the UPS and not lysosomal degradation pathways. Together, these data demonstrate that the genome-edited PLIN2-GFP Huh7 cell line provides a reliable reporter of PLIN2 levels and LD dynamics.

CRISPR-Cas9 screens identify metabolic state-dependent and cell specific regulators of PLIN2-GFP

To systematically profile the genetic factors that regulate PLIN2 levels, we performed genome-wide CRISPR-Cas9 loss-of-function screens under basal and lipolytic (i.e., triacsin C treated) conditions (Figure 1L). Cas9 expressing PLIN2-GFP reporter cells were infected

with a lentiviral sgRNA library containing 10 sgRNAs per gene[27,28] and the top and bottom 30 percent of PLIN2-GFP fluorescent cells were isolated by FACS. For the lipolysis screen, cells were pretreated with triacsin C for 24 hr prior to FACS. The high and low GFP fluorescent cells represent cells in which gene disruption increased or decreased PLIN2-GFP levels, respectively. Following deep sequencing of PCR-amplified library barcodes, sgRNA enrichment was analyzed using Cas9 high-Throughput maximum Likelihood Estimator (casTLE)[27,28]. Employing a 10 percent false discovery rate (FDR), we identified 192 significant gene hits in the basal screen and 275 significant gene hits in the lipolytic screen (Table S1, Figure S1H,I). *PLIN2* itself was identified as a hit since disruption of the endogenous gene reduces PLIN2-GFP expression (Figure S1H,I), and many canonical LD regulators were identified as high-confidence hit genes with strong effects on PLIN2-GFP abundance (Figure S1H,I), consistent with the reciprocal stabilization of PLIN2 and LDs.

To validate our hits, we performed a set of high coverage batch retest screens, which are known to reduce false positives and false negatives[29–32]. For these screens, we synthesized a custom sgRNA library (10 sgRNAs per gene) targeting genes passing a 10% FDR cutoff from our genome-wide CRISPR screens, genes encoding proteins present in prior LD proteomic analyses[33], and selected genes of interest with roles related to lipid metabolism (Figure S1J). In total, this new “Lipid Droplet and Metabolism” sgRNA library contains 13,920 sgRNAs with 11,920 gene-targeting sgRNAs and 2,000 negative control sgRNAs (Figure S1J; Table S2). PLIN2-GFP cells were infected with the custom sgRNA library and duplicate high coverage screens performed under basal and lipolytic conditions, as described for the genome-wide screen (Figure 1L). The batch retest screens resulted in higher gene effects (a score of the phenotype strength) and gene scores (a confidence metric) relative to the genome-wide screens (Figure 1M,N; Figure S1H,I), strongly correlated with the genome-wide screens (Figure S1K,L), identified expected LD regulatory genes (Figure 1M,N; Figure S2A), and further highlighted differential gene effects under basal and lipolytic conditions (Figure 1M,N).

Enzymes involved in nearly every step of neutral lipid synthesis were identified (Figure 2A). Depletion of enzymes that mediate neutral lipid synthesis reduced PLIN2-GFP, including the *de novo* fatty acid synthesis enzymes *ACACA*, *ACLY*, and *FASN*, the fatty acid desaturase *SCD*, the acyl-CoA synthetase *ACSL3*, the glycerol-3-phosphate acyltransferase *AGPAT6* (also known as GPAT4) and its activator *CHP1*, and the diacylglycerol acyltransferase *DGAT2* (Figure 2A). Conversely, disruptions in genes involved in neutral lipid degradation increased PLIN2-GFP, including *PNPLA2* and *ABHD5*, while the disruption of the PNPLA2 inhibitor *HILPDA* reduced PLIN2-GFP (Figure 2A).

A cellular map of the top gene hits from the batch retest screens provides a visual representation of selected high-confidence PLIN2 regulators, highlighting expected regulators of LD biology such as neutral lipid synthesis enzymes as well as numerous genes with no prior connection to LD metabolism or PLIN2 regulation (Figure 2C). Several genes that comprise the SREBP pathway were identified, including *SREBF1/2*, *SCAP*, *INSIG1, and MBTPS2* (Figure 2C). We validated these results for three of the genes, finding that targeted disruption of *INSIG1* increased PLIN2-GFP while depletion of *MBTPS2* or *SCAP* reduced PLIN2-GFP (Figure S2B–E). Although Huh7 LDs primarily contain TAG, multiple

genes involved in cholesterol metabolism were also observed as PLIN2 regulators (e.g., *LSS*, *SQLE*, *SOAT1*, *FDFT1*). These cholesterol metabolic genes were distributed across the cholesterol synthesis pathway (Figure S2F) and may influence PLIN2 abundance by regulating SREBP signaling or by contributing cholesteryl esters that are sequestered in LDs.

We detected a remarkable number of genes involved in mitochondrial biology (Figure 2C). In all cases, the disruption of these genes increased PLIN2-GFP (Figure 2C). Particularly striking was the enrichment of genes within the electron transport chain (Figure 2C). To validate this relationship, we tested the effects of small molecule inhibitors of the electron transport chain. The complex I inhibitor rotenone and the ATP synthase inhibitor oligomycin A increased neutral lipids (Figure S2G,H). In contrast, the carnitine palmitoyltransferase I (CPT1) inhibitor etomoxir had no effect on lipid accumulation (Figure S2I). These data argue that the increase in neutral lipids following electron transport chain inhibition is not simply due to reduced fatty acid oxidation. An alternative is that the increase in LDs reflects a response to the induction of mitochondrial stress pathways, as LD biogenesis is known to increase in response to diverse cellular stresses[20,34–36]. Interestingly, many enzymes involved in the mitochondrial fatty acid synthesis (mtFAS) and lipoic acid synthesis pathways were also identified (Figure 2B,C). While disruption in the cytosolic fatty acid synthesis pathway reduced PLIN2-GFP, likely by reducing the production of *de novo* fatty acids required for neutral lipid synthesis, the disruption of the mitochondrial fatty acid synthesis pathway increased PLIN2-GFP (Figure 2B,C). The mitochondrial fatty synthesis pathway generates the eight-carbon saturated fatty acid caprylic acid (octanoic acid), which is converted into lipoic acid for the lipoylation of several important mitochondrial enzymes, such as pyruvate dehydrogenase. Several components of the pyruvate dehydrogenase complex were detected as high confidence hits – *PDHA1*, *PDHB*, *DLAT*, and *DLD* (Figure 2B,C). The mtFAS pathway also generates longer acyl chains and has roles in regulating electron transport chain assembly and function, independent of protein lipoylation[37]. While the role of the mtFAS pathway in controlling electron transport function may contribute to our observed PLIN2-GFP phenotypes, the identification of lipoic acid synthetase *LIAS* and both lipoyltransferases, *LIPT1* and *LIPT2,* suggests that mitochondrial enzyme lipoylation is involved. Further studies will be necessary to understand the relationship between mitochondrial function and neutral lipid storage.

To explore the generalizability of our findings, we performed an additional set of CRISPR-Cas9 screens in the hepatocellular carcinoma cell line HepG2 and renal cell carcinoma cell line 786-O. Genome-edited PLIN2-GFP reporter cell lines were generated using CRISPR-Cas9 dependent homologous recombination. Western blotting indicated that the HepG2 PLIN2-GFP reporter cell line is heterozygous, with at least one allele modified with GFP and one allele unmodified (Figure S3A). The 786-O PLIN2-GFP reporter cell line is homozygous, with all PLIN2 tagged with GFP (Figure S3B). PLIN2-GFP was easily detected under basal conditions in HepG2 cells (Figure S3C). However, PLIN2-GFP levels were much lower in the 786-O cells, and PLIN2-GFP was only observed after treating the cells with oleate (Figure S3D), likely reflecting differences in PLIN2 expression, stability, or LD amount between the HepG2 and 786-O cells. Employing these new PLIN2-GFP reporter cell lines, we performed duplicate screens using our Lipid Droplet and Metabolism

sgRNA library (Figure 2D,E; Table S1). As expected, we observed a comparable genetic modifier profile between Huh7 and HepG2 cells, which are both hepatocellular carcinoma cell lines (Figure 1M; Figure 2D,F–J). Moreover, we identified several core regulators across all three cell lines, including regulators of lipid synthesis (e.g., *ACACA*, *CHP1*, *DGAT2*, and *SCD*), and degradation (e.g., *PNPLA2*, *ABHD5*, and *HILPDA*), as well as regulators of the mTOR pathway (Figure 2F,G). The screens also revealed numerous intriguing differences. For example, Huh7 and HepG2 cells demonstrated opposite requirements for *INSIG1* and *INSIG2* (Figure 2H). Additionally, while *CHP1* and *DGAT2* were necessary for all cell lines, Huh7 and HepG2 required *AGPAT6*, while 786-O cells demonstrated stronger requirements for *AGPAT9* (Figure 2F). HepG2 and Huh7 cells exhibited stronger regulation of PLIN2-GFP by mitochondria-associated genes (Figure 2I; Figure S3F), including genes involved in the electron transport chain and mitochondrial fatty acid synthesis, suggesting a unique relationship between mitochondria and neutral lipid storage in hepatocyte-derived cell lines. HepG2 and Huh7 also show similar requirements for ER-associated degradation (ERAD) related genes (Figure 2J). Analysis of transcriptional regulation (Figure S3E) and sterol metabolism (Figure S3G) also revealed interesting relationships, such as the importance of BAP1 in HepG2 and 786-O cells and of HDAC3 in Huh7 and 786-O cells. Together, our genome-wide and batch retest screens provide an extensive inventory of genetic modifiers that govern PLIN2 levels in different cell types and under different metabolic conditions.

MARCH6 regulation of neutral lipid storage in LDs indirectly stabilizes PLIN2

PLIN2 levels are post-translationally controlled by its degradation via chaperone-mediated autophagy[23,38] and the ubiquitin-proteasome system[24–26]. In cell lines that have low amounts of LDs, uninserted PLIN2 is degraded through a mechanism involving the ER-resident E3 ubiquitin-ligase MARCH6 (also known as TEB4)[25]. We detected several sgRNAs targeting *MARCH6* and its cognate E2 ubiquitin-conjugating enzyme *UBE2J2* under basal (Figure 3A,D) and lipolytic conditions (Figure S4A,B), identifying these genes as high confidence PLIN2 regulators and suggesting that MARCH6 and UBE2J2 cooperate to control PLIN2 stability in LD-rich Huh7 cells. Indeed, the disruption of *MARCH6* or *UBE2J2* with 3 or 2 independent sgRNAs, respectively, increased PLIN2-GFP levels under basal conditions and more strongly under triacsin C treated conditions (Figure 3B,C,E,F). Due to the lack of effective anti-MARCH6 antibodies, MARCH6 depletion was confirmed by genome sequencing and the accumulation of its known substrate squalene monooxygenase (SQLE)[39–41] (Figure S4C), and UBE2J2 KO was confirmed by immunoblotting (Figure S4D).

To characterize the role of MARCH6 in regulating PLIN2, we analyzed the turnover kinetics of PLIN2-GFP and endogenous, untagged PLIN2 in control and MARCH6 KO ($MARCH6^{KO}$) cells during a 24 hr triacsin C treatment. PLIN2-GFP levels were higher in $MARCH6^{KO}$ cells relative to Cas9 control cells at all time points throughout the triacsin C treatment time course (Figure 3G,H). However, quantification of the PLIN2-GFP turnover rate after normalization to the initial higher levels (i.e., at time 0) indicates that the rate of PLIN2-GFP degradation during lipolysis is mostly unaltered in $MARCH6^{KO}$ cells (Figure 3I). Endogenous, untagged PLIN2 responded similarly to the GFP-tagged protein, showing

increased levels in the MARCH6^{KO} cells and an unaltered rate of clearance (Figure S4E,F). We considered the possibility that the increase in SQLE, which is a rate-limiting enzyme in cholesterol biosynthesis[39–41], could be responsible for the changes in PLIN2 levels in MARCH6^{KO} cells. However, siRNA-mediated depletion of SQLE had no effect on the levels of untagged PLIN2 or PLIN2-GFP in western blots (Figure 3J) or of PLIN2-GFP levels measured by flow cytometry under basal or triacsin C treated conditions (Figure 3K,L). Together, these data indicate that although MARCH6 affects PLIN2 levels in Huh7 cells, MARCH6 is not required for the clearance of LD-inserted PLIN2 during the lipolytic breakdown of LDs and its effects on PLIN2 are independent of SQLE.

Given the increase in PLIN2 levels in MARCH6^{KO} cells and the high correlation between PLIN2 and LDs, we examined LDs in MARCH6^{KO} cells by confocal imaging (Figure 4A,B). Depletion of MARCH6 in parental Huh7 cells increased endogenous PLIN2 levels (Figure S5A) and the amount of LDs (Figure 4A,B, Figure S5B). Quantification of neutral lipid content by flow cytometry indicated an increase in neutral lipids in MARCH6^{KO} cells in Huh7 and other hepatoma cell lines (HepG2 and Hep3B), but not 786-O and U-2 OS (Figure 4C, Figure S5C–F). To gain insight into the biochemical changes in cellular lipids, we performed untargeted lipidomics on Huh7 MARCH6^{KO} cells. Principal component analysis of the lipidomics data showed a distinct cluster of MARCH6^{KO} cell lines that was well separated from Cas9 control cells (Figure 4D). Consistent with our imaging data showing an increase in neutral lipids stored in LDs, the lipidomics analyses revealed a general increase in TAG species (Figure 4E). These TAG species were diverse in their compositions of conjugated fatty acids, including their degree of unsaturation and number of carbons (i.e., fatty acid chain length) (Figure 4F, Figure S5G). There were also reductions in phosphatidylcholine (PC) as well as increases in phosphatidylinositol (PI), indicating that the effects of MARCH6 on the cellular lipid landscape are not limited to TAG (Figure 4E,F; Figure S5H). The mechanism and significance of the change in PI is unclear. It is possible that the decrease in PC may reflect an increase in flux of glycerolipid precursors into TAG at the expense of phospholipids, as has been observed under certain conditions[42].

To test whether increased PLIN2 in MARCH6^{KO} cells is responsible for the higher neutral lipid levels, we introduced MARCH6 sgRNAs into PLIN2^{KO} cell lines and measured neutral lipid content. As anticipated, loss of PLIN2 reduced neutral lipid content (Figure S5I,J). However, loss of PLIN2 had no effect on the increase in neutral lipid content following MARCH6 depletion (Figure 4G,H, Figure S5K–M). Additionally, depletion of SQLE also had no effect on neutral lipid levels in the MARCH6^{KO} cell line (Figure 4I,J). These findings indicate that the effect of MARCH6 on neutral lipid levels is independent of PLIN2 and SQLE accumulation. These data support a model in which MARCH6 regulates TAG and LD levels, which in turn affect PLIN2 stability. Indeed, other obligate LD proteins that are reciprocally regulated by LD levels are increased in the MARCH6^{KO} cells, including ATGL and CGI-58, which are stabilized by LDs and degraded by the proteasome in the absence of LDs[43–46] (Figure 4K). We noted a modest increase in the ER-resident desaturase SCD1, but not in another ER protein, seipin, nor in the ER-resident cholesterol synthesis enzyme NSDHL. SCD1 is known to enhance LD biogenesis by generating unsaturated fatty acids that are more efficiently incorporated into TAG[47]. SCD1 levels were also increased in the hepatoma cell lines HepG2 and Hep3B, but not 786-O or U-2 OS cell lines (Figure S4G–

J). Depletion of SCD1 using siRNAs resulted in a reduction in the neutral lipid increase observed in MARCH^{KO} cells, suggesting that stabilization of SCD1 may contribute to the increased LDs and PLIN2 stabilization in MARCH6^{KO} cells (Figure 4L; Figure S5N).

To further explore the mechanism, we measured TAG biosynthesis and turnover using a fluorescent fatty acid pulse labeling approach in which the fluorescent fatty acid BODIPY C12[48] was added to cells and its incorporation into TAG measured at several time points (Figure 4M–O, Figure S5O,P). The rate of BODIPY C12 incorporation into TAG was increased in three MARCH6^{KO} cell lines (Figure 4M,N, Figure S5O,P). In contrast, the rate of triacsin C-induced lipolytic breakdown of BODIPY C12-containing TAG was mostly unchanged in the MARCH6^{KO} cell lines (Figure 4M,P). Together, our data indicate that loss of MARCH6 in hepatocyte-derived cell lines indirectly stabilizes PLIN2 on LDs by promoting TAG biosynthesis and an increase in LD amount, potentially by stabilizing factors that promote lipogenesis, such as SCD1.

Parallel screens uncouple transcriptional and post-translational mechanisms of PLIN2 regulation

The screens employing our PLIN2-GFP reporter cell line identified regulators that influence PLIN2 levels through diverse mechanisms – transcriptional, translational, and post-translational. To systematically uncouple these mechanisms of PLIN2 regulation, we engineered a Huh7 reporter cell line in which eGFP and blue fluorescent protein (BFP), separated by a short P2A sequence, were integrated in frame with the C-terminus of endogenous PLIN2 (Figure 5A). The short self-cleaving P2A peptide sequence induces a ribosomal skip and allows BFP to be translated from the same transcript as the PLIN2-GFP fusion protein (Figure 5A). Thus, BFP levels report on PLIN2 transcription and the GFP:BFP ratio reports on post-translational regulation.

The PLIN2-GFP-P2A-BFP reporter cell line exhibited GFP and BFP fluorescence above wild type, parental Huh7 cells (Figure 5B). A single PLIN2-GFP band was detected by immunoblotting at the expected molecular weight (Figure 5C), confirming in-frame insertion of GFP and appropriate cleavage of PLIN2-GFP and BFP at the P2A peptide. siRNA depletion of the PLIN2 transcript led to a reduction in both GFP and BFP (Figure 5D), consistent with BFP expression from the PLIN2 transcript. Oleate-induced LD biogenesis increased and triacsin C-induced lipolysis decreased PLIN2-GFP levels, but not BFP levels (Figure S6A), in agreement with the post-translational regulation of PLIN2-GFP stability by LDs. These data demonstrate the utility of this new reporter cell line in distinguishing between transcriptional and post-translational mechanisms of PLIN2 regulation.

Employing the Huh7 PLIN2-GFP-P2A-BFP reporter cell line, we performed screens using our Lipid Droplet and Metabolism sgRNA library (Figure 5E). Cells were sorted based upon BFP fluorescence to identify transcriptional regulators or upon the ratio of GFP:BFP fluorescence to identify post-translational regulators (Figure 5E, Table S1). As expected, sgRNAs targeting PLIN2 were depleted in both screens (Figure S6B,C). Genes that are directly involved in the biosynthesis and turnover of neutral lipids and LDs were identified in the GFP:BFP screen, including *DGAT2*, *ABHD5*, *ACSL3*, *HILPDA*, *CHP1*, and *AGPAT6*

(Figure 5F,G, Figure S6D,E). These genes were absent in the BFP screen (Figure 5H,I), indicating that they regulate PLIN2 post-translationally. *MARCH6* and *UBE2J2* were also identified as post-translational regulators of PLIN2 (Figure 5G), in agreement with our earlier studies examining their effects on PLIN2 stability (Figure 3). Several interesting novel regulators of PLIN2 were found to act post-translationally (Figure 5F,G,J,K), such as the ER scramblase TMEM41B, which was recently implicated in autophagy and LD regulation[49–51]. Conversely, our screens also identified regulators of PLIN2 expression, which were enriched in genes encoding proteins that localize to the nucleus and function as transcription regulators, such as *HNF1A*, *HNF4A*, *TADA2B*, *NCOA6*, and others (Figure 5H,I,L,M). Interestingly, the SREBP pathway components were identified as post-translational regulators of PLIN2, having little effect on PLIN2 transcription (Figure 5N). These data argue against PLIN2 as a direct SREBP target and support a model in which SREBP primarily influences PLIN2 stability, likely through its role in controlling cellular lipid metabolism. Some genes that clustered within particular processes, such as mitochondrial fatty acid synthesis, sterol metabolism, oxidative phosphorylation, and protein degradation (Figure 5O,P; Figure S6F,G), were detected in both the GFP:BFP and BFP screens, indicating that they have complex roles in regulating both the expression and stability of PLIN2.

To validate this new set of screens, we further analyzed a small set of candidate PLIN2 transcriptional regulators. *HDAC3* and *HNF4A* were detected as high confidence regulators based on the enrichment of several sgRNAs (Figure 6A,E). Depletion of histone deacetylase 3 (HDAC3) in our PLIN2-GFP-P2A-BFP reporter cells (Figure S7A) increased GFP and BFP levels (Figure 6B), and parental Huh7 cells depleted of HDAC3 (Figure S7B) exhibited increased neutral lipid staining (Figure 6C) and increased PLIN2 transcript levels (Figure 6D). These data indicate that HDAC3 suppresses PLIN2 expression and are consistent with the known epigenetic regulation of hepatic lipid metabolism by HDAC3[52]. Indeed, PLIN2 is upregulated in *HDAC3* null mice, and these mice exhibit hepatic steatosis that can be suppressed by PLIN2 depletion with anti-sense oligos[52]. Conversely, depletion of hepatocyte nuclear factor 4-alpha (HNF4A) in PLIN2-GFP-P2A-BFP reporter cells (Figure S7C) reduced GFP and BFP (Figure 6F), and parental Huh7 cells depleted of HNF4A (Figure S7D) exhibited decreased neutral lipid staining (Figure 6G) and reduced PLIN2 transcript levels (Figure 6H). Similarly, depletion of HNF4A in HepG2 also led to a reduction in neutral lipids (Figure S7E,F). Confocal imaging further validated the changes in neutral lipids (Figure 6I–K, Figure S7G). HNF4A is a transcription factor that regulates hepatocyte differentiation through its role in controlling the expression of numerous hepatocyte genes associated with glucose and lipid metabolism[53,54]. The reduced LDs in $HNF4A^{KO}$ cells may be due to reduced maintenance of hepatocyte identity. Consistent with this possibility, immunoblotting demonstrates a reduction in the hepatocyte marker FABP1 (Figure S7D), and phalloidin fluorescence imaging indicates a remarkable alteration in morphology (Figure 7L), with a loss in cobblestone morphology and organized cortical actin staining and an increase in spindle-shaped cells. Moreover, depletion of two additional transcription regulators (*TADA2B* and *SUPT20H*) also led to the predicted reductions in BFP fluorescence, consistent with roles in regulating PLIN2 expression (Figure S7H–M).

Thus, the screens in the PLIN2-GFP-P2A-BFP reporter cells identify transcriptional and post-translational PLIN2 regulators.

CRISPRlipid: A data commons for functional genomics screens related to lipid biology

To facilitate the exploration of the functional genomics data generated in this study, we built CRISPRlipid (http://crisprlipid.org/), an online data commons (Figure 7). This resource provides a community site for data from functional genomics screens related to lipid biology, such as lipid storage and breakdown, lipid signaling, membrane and organelle regulation, and lipotoxicity. CRISPRlipid employs a similar user interface and is conceptually similar to CRISPRbrain[55], which focuses on genetic screens in differentiated cell types. Upon its launch, CRISPRlipid contains 23 CRISPR screens related to lipid biology. These screens include the PLIN2-GFP and PLIN2-GFP-P2A-BFP screens described in this study, as well as data from published screens from our lab and other labs that identify genetic modifiers of oxidative lipid damage and ferroptosis[56,57], palmitate-induced toxicity[58], lysosomal cholesterol and bis(monoacylglycerol)phosphate (BMP) levels[59], ceramide-induced toxicity[60], LDs in mouse microglia[20], and glycosylphosphatidylinositol biosynthesis[61]. CRISPRlipid allows users to browse screens, enables rapid visualization of screen data as interactive volcano plots and rank plots, and generates pairwise comparisons between different screens (Figure 7A). Graphs within CRISPRlipid are interactive, and genes of interest or data from the entire screen can be selected and exported for offline analysis.

One of the most powerful features within CRISPRlipid is the “compare simple screens” tool, which presents pairwise comparisons between different screens as a scatter plot (Figure 7A). These comparisons are possible because all screens in CRISPRlipid are analyzed using the same analysis pipeline. As an illustrative example of how this feature can be useful, we employed CRISPRlipid to compare the genetic modifiers of PLIN2-GFP levels under basal conditions with the genetic modifiers of PLIN2-GFP levels under lipolytic conditions (Figure 7B), of palmitate toxicity (Figure 7C), and of accessible cholesterol (Figure 7D). As anticipated, there was a strong correlation between genes that regulate PLIN2-GFP levels under basal and lipolytic conditions, and depletion of genes that regulate LD biogenesis (e.g., *ACSL3* and *DGAT2*) or suppress lipolysis (e.g., *HILPDA*) had strong negative effects on PLIN2-GFP levels under basal conditions but no effect under lipolytic conditions (Figure 7B). Interestingly, several factors that positively influence PLIN2-GFP levels and LD biogenesis, *ACSL3*, *CHP1*, and *AGPAT6*, also promoted palmitate toxicity (Figure 7C). This might be unexpected because LDs suppress saturated fatty acid toxicity by mediating their sequestration in TAG[47]. However, ACSL3, CHP1, and AGPAT6 are also involved in early steps of glycerolipid biosynthesis, regulating the biosynthesis of TAG and glycerophospholipids. High amounts of saturated fatty acids in glycerophospholipids reduce membrane fluidity and increase ER stress and cell death. The results in Figure 7C indicate that the role of ACSL3, CHP1, and AGPAT6 in incorporating saturated fatty acids into phospholipids is dominant over their protective role in sequestering saturated fatty acids in LDs, consistent with recent findings[58,62]. *ACACA*, *SETD1B*, and *UBE2G2* show a similar functional relationship as *ACSL3*, *CHP1*, and *AGPAT6* (Figure 7C), raising the possibility that they play analogous roles in regulating fatty acid flux into glycerolipids. A comparison

of the genetic modifiers of PLIN2-GFP levels and accessible cholesterol highlights genes that selectively influence PLIN2-GFP (e.g., *ACSL3*, *DGAT2*) and cholesterol (e.g., *NPC1*, *MYLIP*, *Rab7*, *c18orf8*) along the axes (Figure 7D). The comparison also identifies *CHP1* and *AGPAT6* as shared regulators of PLIN2-GFP and cholesterol (Figure 7D), raising the possibility that impaired glycerolipid biosynthesis leads to an increase in accessible cholesterol levels. These three pairwise comparisons (Figure 7B–D) provide examples of how CRISPRlipid can be used to uncover unexpected functional relationships between genes and to generate hypotheses of cellular lipid regulation that can be experimentally explored in future studies.

DISCUSSION

In this study, we developed and employed a set of genome-edited PLIN2-GFP reporter cell lines in a series of CRISPR-Cas9 loss-of-function screens to globally profile genes that regulate PLIN2 abundance in different cell types and under multiple metabolic conditions. Our functional genomics data provide a comprehensive inventory of genes that regulate PLIN2 levels and reveal their mechanism of regulation as transcriptional or post-translational. Given the reciprocal relationship of PLIN2 and LDs, these data also provide a wealth of candidate regulators of LDs and neutral lipids. We identified the expected regulators of LD biogenesis and turnover, as well as new regulators and processes that were not previously connected with PLIN2, such as the electron transport chain, mitochondrial fatty acid synthesis, and protein lipolyation pathways. We validated the effects of selected transcriptional regulators, such as *HNF4A* and *HDAC3*, and post-translational regulators, such as *MARCH6*, *UBE2J2*, and enzymes within the SREBP pathway, supporting the strength and confidence in our resource.

The identification of MARCH6 and its cognate E2 enzyme UBE2J2 as post-translational regulators of PLIN2 is in line with a previous study that reported MARCH6 ubiquitination and degradation of uninserted PLIN2[25]. In cell types lacking LDs, MARCH6 was reported to recognize an acetylation-dependent degradation signal at the PLIN2 N-terminus, which functions as an N-end rule degron[25]. Although we find that MARCH6 affects PLIN2 levels and LDs in Huh7 cells and other hepatocellular carcinoma cell lines (HepG2 and Hep3B), our data indicate that MARCH6 indirectly regulates PLIN2 protein stability through its effects on LD abundance. Indeed, loss of MARCH6 still increases LDs in a PLIN2 KO cell line, and MARCH6 KO does not affect the rate of PLIN2 clearance during the lipolytic breakdown of LDs. We further find that MARCH6 KO increases the rate of TAG biosynthesis and has no effect on TAG lipolysis. Thus, the simplest model is that MARCH6 mediates the ubiquitination and degradation of one or more enzymes involved in neutral lipid synthesis or LD biogenesis. Analysis of the MARCH6^{KO} cells indicates a modest stabilization of SCD1, which is known to stimulate LD biogenesis by increasing the amount of unsaturated fatty acids, and depletion of SCD1 partially reduced LD abundance in MARCH6^{KO} cells. Whether SCD1 is a direct substrate of MARCH6-catalyzed ubiquitin-dependent degradation and whether other substrates contribute to the increase in LDs remains to be determined. The question of how LD inserted PLIN2 is degraded during the lipolytic consumption of LDs also remains open. It was recently shown that the E3 ligases UBR1 and UBR2 play redundant roles in promoting PLIN2 proteasomal

degradation in hepatocytes[63]. It is possible that UBR1 and UBR2 may contribute to PLIN2 degradation under lipolytic conditions. One limitation of CRISPR-Cas9 loss-of-function screens is the inability to identify genes that can be readily compensated for by redundant pathways. Indeed, TRC8 compensates for the loss of MARCH6 in the degradation of certain substrates[64]. TRC8 was not detected in our screens, but it remains possible that TRC8 or other E3 ligases could partially compensate for the loss of MARCH6. It is notable that induced PLIN2 degradation through overexpression of a constitutively active form of UBR2 was sufficient to suppress hepatic steatosis[63], demonstrating the potential therapeutic value of regulating PLIN2 degradation.

With the explosion in “big data”, a major challenge that remains is how to best make data accessible to facilitate discovery. To promote accessibility, exploration, and comparison of data generated from functional genomic screens, we established CRISPRlipid as a new, open access online data commons for the lipid biology community. We envision CRISPRlipid as an open online portal that provides the scientific community with a resource of functional genomics screen data related to diverse aspects of lipid biology, including (but not limited to) neutral lipid storage, lipid biosynthesis and breakdown, lipotoxicity, lipid signaling, lipid enzyme activity, and membrane homeostasis and remodeling. The strength of this site will increase as additional data are deposited from new screens in different cell types and under different conditions, and we invite the research community to contribute functional genomics datasets related to lipid biology (broadly defined) to CRISPRlipid. The integration of systems-level datasets provides a tool for the community to gain a comprehensive understanding of the functional networks that govern cellular lipid homeostasis across diverse cell types and conditions.

LIMITATIONS OF THE STUDY

Our study employed a limited number of cell types and metabolic conditions. Further studies in cells derived from other tissues and under different metabolic states and stress conditions are bound to reveal LD functions and mechanisms of regulation. In addition, although PLIN2 levels generally correlate with neutral lipid and LD abundance, it is possible that similar screens using neutral lipid stains could identify unique sets of genetic modifiers. It is also important to note that other PLIN family members and LD proteins are functionally distinct and are likely subject to different mechanisms of regulation. Several questions remain regarding the mechanism by which MARCH6 regulates neutral lipid biosynthesis. Our data support a plausible model in which MARCH6 mediates the degradation of TAG synthesis enzymes or regulators (e.g., SCD1) to influence TAG biosynthesis rates. However, further studies will be necessary to demonstrate which proteins are targeted by MARCH6, presumably for ubiquitin-dependent proteasomal clearance, though non-proteasomal mechanisms of regulation are also possible. Finally, our study identified numerous cellular processes that impact PLIN2 and LD abundance, with the most enriched genes being related to mitochondrial fatty acid synthesis and the electron transport chain. Initial studies with small molecule inhibitors validated a connection between the electron transport chain and LDs, but additional research is necessary to fully understand the molecular underpinnings of this relationship and its physiological significance.

STAR METHODS

Resource availability

Lead contact—Further information and requests for resources and reagents should be directed to and will be fulfilled by the lead contact, James Olzmann (olzmann@berkeley.edu).

Materials availability—All unique/stable reagents generated in this study are available from the lead contact with a completed Materials Transfer Agreement. The custom Human Lipid Droplet and Metabolism sgRNA Library was deposited at Addgene (Addgene, 191535).

Data and code availability

- All data reported in this paper will be shared by the lead contact upon request.
- This paper does not report original code.
- Any additional information required to reanalyze the data reported in this paper is available from the lead contact upon request.

EXPERIMENTAL MODEL AND STUDY PARTICIPANT DETAILS

Cell lines and culture conditions—Huh7, U-2 OS, and HEK293T cells were cultured in DMEM containing 4.5 g/l glucose and L-glutamine (Corning) supplemented with 10% fetal bovine serum (FBS) (Thermo Fisher Scientific and Gemini Bio Products). HepG2 and 786-O cells were cultured in RPMI 1640 medium (Gibco) containing L-glutamine supplemented with 10% FBS. Hep3B cells were cultured in EMEM (ATCC, 50-188-268FP) containing L-glutamine supplemented with 10% FBS. All cells were maintained at 37°C and 5% CO2.

Generation of endogenously labeled PLIN2-GFP reporter cells in Huh7—Endogenous PLIN2 in Huh-7 human hepatocellular carcinoma cells was labeled with a C-terminal AGSGA (flexible linker)-eGFP-S-tag (KETAAAKFERQHMDS) with an internal ribosome entry site (IRES) to allow parallel mTag BFP expression introduced using CRISPR-Cas9 homology-directed repair. The donor construct was produced by first amplifying the target homology region from Huh7 genomic DNA with the following outer nested primers: ns_PLIN2_C_HDR_For and ns_PLIN2_C_HDR_Rev, followed by the phosphorylated inner nested primers: PLIN2_HDR_For and PLIN2_HDR_Rev. The phosphorylated fragment was then ligated into a pM575 backbone. A 2062 bp fragment encoding an AGSGA-GFP-S IRES BFP cassette was introduced into the homology region of the intermediate plasmid using polymerase incomplete primer extension cloning with the insert primers: pI_PLIN2_C_For and pI_PLIN2_C_Rev and vector primers: pV_PLIN2_C_For and pV_PLIN2_C_Rev to yield the complete pPLIN2-GFP-S-IRES-BFP HDR donor construct, which has 1045 bp and 1231 bp genomic DNA homology arms on either side of the 2062 bp labelling cassette.

CRISPR guide oligos PLIN2_C_g1_For and PLIN2_C_g1_Rev were annealed and ligated into a px330 backbone to yield px330-PLIN2 C g1.

Huh-7 cells were transfected with 2.67 μg of px330-PLIN2 C CRISPR guide 1 and 5.33 μg of pPLIN2-GFP-S-IRES-BFP HDR donor construct with 8 μL of XtremeGENE HP and treated with 1 μM SCR7 (DNA ligase IV inhibitor that blocks nonhomologous end-joining) after 6 hr. After 72 hr, the media was replenished and supplemented with 1 μM SCR7. After a further five days, the population was enriched for 0.05% of cells exhibiting green fluorescence using fluorescence-activated cell sorting (FACS). Cells were sorted another three times to enrich for GFP^+ cells and eliminate non-GFP^+ wild type cells from the population. Primer sequences are listed in Table S2.

Generation of endogenously labeled PLIN2-GFP-P2A-BFP (Huh7) and PLIN2-GFP (HepG2 and 786-O) reporter cells—To generate the PLIN2 knock-in donor plasmid, 500-bp homology arms flanking the PLIN2 stop codon were amplified from Huh7 genomic DNA and inserted into pUC19. To introduce the GFP-P2A-BFP insert, 15-bp overlaps with each of the PLIN2 homology arms were introduced to the codon optimized GFP-P2A-BFP insert (gBlock synthetic DNA, Integrated DNA Technologies). This insert was then cloned in frame of with the PLIN2 stop codon using restriction enzyme-independent fragment insertion by megaprimer cloning. To create the GFP insert, the P2A-BFP insert was deleted by inverse PCR using phosphorylated primers. The protospacer adjacent motif site that corresponds to *PLIN2* sgRNA was subsequently mutated in the donor sequence using site-directed mutagenesis primers to prevent cutting of the integrated donor sequence by Cas9.

CRISPR guide RNA (sgRNA) sequences targeting PLIN2 were designed using the CRISPR guide design tool by Benchling (https://www.benchling.com) and can be found in Table S2. Underlined nucleotides show the overhangs introduced into oligonucleotides that are necessary for cloning into the BbsI restriction site of vector px330 (Addgene, 42230).

PLIN2 GFP-P2A-BFP (Huh7) and PLIN2-GFP (HepG2 or 786-O) knock-in lines were generated by co-transfection of each donor pUC19 plasmid and px330 encoding *PLIN2* sgRNA guide 1 at a 3:1 w/w ratio using X-tremeGENE HP. 6hr post-transfections, cells were treated and maintained in 1μM SCR7 for one week. GFP-P2A-BFP and GFP reporter cells were enriched via FACS. 786-O cells were pre-treated overnight in 100 μM oleate-BSA, while Huh7 or HepG2 cells were untreated prior to FACS.

Generation of CRISPR-Cas9 Genome Edited Cell Lines—For CRISPR-Cas9 screens and individual knockout cell lines in Huh7 (wild type, PLIN2-GFP, PLIN2-GFP-P2A-BFP), HepG2 (wild type, PLIN2-GFP), U-2 OS (wild type), 786-O (wild type, PLIN2-GFP), and Hep3B (wild type) cells stably expressing Cas9 were generated by infection with lentiCas9-Blast, a gift from F. Zhang (Addgene, 52962). Cells were selected in medium containing blasticidin (4 μg/ml in Huh7 and U-2 OS; 6 μg/ml in HepG2; 8 μg/ml in 786-O; 10 μg/ml in Hep3B) until uninfected control cells were dead. Active Cas9 expression was validated by flow cytometry analysis following infection a self-cleaving mCherry plasmid (pMCB320 containing mCherry and an sgRNA targeting the mCherry gene).

All knockout cell lines (in Huh7, HepG2, Hep3B, U-2 OS, and 786-O cells) were generated using the pMCB320 plasmid, a gift from M. Bassik (Addgene, 89359). Guide sequences (see Table S2) were selected from the Bassik Human CRISPR Knockout Library (Addgene 101926, 101927, 101928, 101929, 101930, 101931, 101932, 101933, 101934) based on enrichment and significance in CRISPR-Cas9 screens. Guide sequences were cloned into pMCB320 using the restriction enzymes BstXI and BlpI.

In the Huh7 cell line, individual knockouts were generated in wild type ($HDAC3^{KO}$, $HNF4A^{KO}$, $MARCH6^{KO}$, $PLIN2^{KO}$), PLIN2-GFP ($ABHD5^{KO}$, $INSIG1^{KO}$, $MARCH6^{KO}$, $MBTPS2^{KO}$, $PNPLA2^{KO}$, $SCAP^{KO}$, $UBE2J2^{KO}$), and PLIN2-GFP-P2A-BFP ($HDAC3^{KO}$, $HNF4A^{KO}$, $SUPT20H^{KO}$, $TADA2B^{KO}$) cells. Knockouts in HepG2 ($MARCH6^{KO}$, $HNF4A^{KO}$), Hep3B ($MARCH6^{KO}$), U-2 OS ($MARCH6^{KO}$), and 786-O ($MARCH6^{KO}$) cells were generated in the wild type background. Control cell lines were generated using the pMCB320 plasmid expressing sgRNAs targeting genomic locations with no annotated function (safe-targeting guide; sgSAFE #5784) or sgRNAs with no binding sites in the genome (sgNONE #2717) as described previously[28].

To generate lentiviral particles, sgRNA-containing pMCB320 plasmids were co-transfected with third-generation lentiviral packaging plasmids (pMDLg/pRRE, pRSV-Rev, and pMD2.G) into HEK293T cells. Media containing lentivirus was collected 48 or 72 hr after transfection, filtered, and then used to infect cells stably expressing Cas9. After 72 hr of growth, infected cells were selected in media containing puromycin (2 μg/ml in Huh7, HepG2, and 786-O; 1 μg/ml in Hep3B and U-2 OS) or 0.25 μg/ml hygromycin B (for Huh7 $PLIN2^{KO}$ cells) until over 90% cells were mCherry positive and all uninfected control cells were dead. Huh7 $MARCH6^{KO}$ (in wild type and PLIN2-GFP backgrounds) and Huh7 $PLIN2^{KO}$ clones were isolated using serial dilutions. Knockout efficiencies were confirmed via immunoblotting and/or genomic DNA sequencing.

METHOD DETAILS

Genomic DNA Sequencing and Indel Analysis—PCR primers were designed using the IDT PrimerQuest Tool (Integrated DNA Technologies) and can be found in Table S2. Briefly, primers were designed to flank the predicted Cas9 cut site, with the forward primer ~100bp upstream of the cut site.

For the genomic DNA extraction, cells were washed twice and scraped off plates in cold DPBS and pelleted at 500× g for 5 min. Genomic DNA was extracted from cell pellets and purified using the Qiagen Blood Mini Kit (Qiagen, 51104) according to manufacturer's instructions.

PCR was performed on an Applied Biosystems Thermal Cycler using Q5 High-Fidelity 2X Master Mix (New England Biolabs, M0492S). PCR conditions were as follows: 1× 98 °C (2 min); 30× 98 °C (30 sec), 57.5 °C (30 sec), 72 °C (60 sec); 1× 72°C (3 min).

Amplicons were separated on 2% agarose-TAE gels and purified using the QIAquick Gel Extraction Kit (Qiagen, 28706). Amplicons were sequenced at QuintaraBio, and sequences

were assessed for indels using the ICE CRISPR Analysis Tool (Synthego Performance Analysis, ICE Analysis. 2019. v2.0).

Immunoblotting—Cells were washed 2x in DPBS, lysed in 1% SDS, heated at 65 °C, and sonicated at 15% amplitude for 10–20 seconds. Protein concentrations were determined and normalized using the bicinchoninic acid (BCA) protein assay (Thermo Fisher Scientific, 23225). Equal amounts of protein by weight were combined with Laemmli buffer, boiled for 5 min at 95 °C, separated on 4–20% polyacrylamide gradient gels (Bio-Rad Laboratories) and transferred onto nitrocellulose membranes (Bio-Rad Laboratories). Membranes were incubated in 5% nonfat milk in PBS with 0.1% Tween-20 (PBST) for 30 min to reduce nonspecific antibody binding. Membranes were then incubated for at least 2 hr in PBST containing antibodies diluted in 1% BSA, followed by incubation for at least 1 hr in fluorescence-conjugated secondary antibodies diluted in PBST containing 5% nonfat milk. Immunoblots were visualized on a LI-COR imager (LI-COR Biosciences), and Fiji/ImageJ was used for quantification of protein levels.

Fluorescence Microscopy—For widefield microscopy, Huh7 PLIN2-GFP cells were grown in 4-well Nunc™ Lab-Tek™ II Chambered Coverglass (Borosilicate Glass 1.5; Thermo Fisher Scientific, 155360). For live cell imaging of Huh7 PLIN2-GFP cells, cells were incubated in the presence of 200 μM oleate-BSA complex for 24 hr. Lipid droplets were stained with 0.5 μM Lipi-Deep Red (Dojindo) for 2 hours and nuclei were stained with 5 μg/mL Hoeschst 33342 for 30 minutes. Prior to imaging, cells were washed 2x with DPBS and imaged in fresh medium supplemented with 10% FBS lacking phenol red. Live cells were imaged using a Zeiss Axio Observer 7 fitted with a 63X oil objective using DAPI, GFP, and Cy-7 filters. Cells were imaged at 37 °C with 5% CO2. Z-stacks of 0.5-μm thickness were acquired.

For fixed cell imaging of HNF4A^{KO} cells, cells were grown in 12-well plates on glass coverslips coated with poly-L-lysine. Cells were washed 3x with DPBS, fixed for 15 min in DPBS containing 4% (w/v) paraformaldehyde and washed 3x again with DPBS. Cells were permeabilized for 15 min with 1% BSA in DPBS containing 0.1% Triton X-100 and then washed 3x with DPBS. Cells were incubated in Alexa Fluor 488 Phalloidin (Thermo Fisher Scientific, A12379) in 1% BSA in DPBS for 1 hr in the dark. Cells were washed and then incubated in staining buffer containing DAPI for 20 min in the dark. Cells were washed 3x with DPBS and coverslips mounted on 1 mm glass slides using Fluoromount-G (SouthernBiotech, 0100-01). Cells were imaged using a Zeiss Axio Observer 7 fitted with a 40X objective using DAPI and Alexa Fluor 488 filters. Z-stacks of 0.3-μm thickness were acquired.

For live cell confocal microscopy, Huh7 MARCH6^{KO} cells were grown in 24-well glass bottom plates (170 μm coverglass bottom; Eppendorf, 0030741021; Cellvis, P24-1.5H-N). Cells were either untreated or incubated in 200 μM oleate-BSA complex or 1 μg/ml triacsin C for 8 hours. Lipid droplets were stained with 0.5 μM Lipi-Green (Dojindo) for 2 hours and nuclei were stained with 5 μg/mL Hoeschst 33342 for 30 minutes. Prior to imaging, cells were washed 2x with DPBS and imaged in fresh medium supplemented with 10% FBS lacking phenol red. Live cells were imaged using an Opera Phenix Plus

High-Content Screening System (Perkin Elmer) confocal microscope equipped with a 63X water immersion objective using DAPI and GFP filters. Cells were imaged at 37 °C with 5% CO_2. Z-stacks of 0.5-μm slices were acquired.

Images were merged and brightness and contrast adjusted using Fiji/ImageJ (https://imagej.net/software/fiji/).

LDs were quantified by creating a custom analysis sequence using Harmony High Content Image Analysis Software, v4.9 (Perkin Elmer). For each field, maximum projection Z-stacks were processed with advanced flatfield correction. Nuclei and cytoplasm were defined using the DAPI and eGFP channels, respectively, and border cells were automatically excluded from analyses. LDs were defined using the "Find Spots" building block (Lipi-Green stain, eGFP channel), thresholding for size, intensity, and roundness. For each cell, lipid droplet number and area (μm2) were quantified. LD quantification data were graphed and analyzed in Prism 9 (GraphPad).

Flow Cytometry—For flow cytometry analysis of PLIN2-GFP levels, Huh7, HepG2, and 786-O cells were seeded in 6-well plates. If subjected to treatments, cells were treated the next day with 1 μg/ml triacsin C, 200 μM oleate-BSA complex, or DMSO for 24 hr. Cells were dissociated from plates using TrypLE Express (Gibco) and resuspended in DMEM containing 10% FBS. Cells were pelleted by centrifugation at 300× g for 3 min, washed 1x and resuspended in DPBS. For neutral lipid analysis, cells were incubated with 100 μM of the neutral lipid stain MDH[66] (Abcepta) for 30 min on ice prior to pelleting at 300× g. Cells were washed with DPBS and resuspended in DPBS prior to flow cytometry analysis.

For all flow cytometry assays, fluorescence was analyzed using an LSR Fortessa (BD Biosciences). The following filter sets were used: FITC (GFP, BODIPY 493/503), Pacific Blue (BFP, MDH), and Texas-Red (mCherry, propidium iodide). FlowJo Software (BD Biosciences) was used to quantify fluorescence and generate representative histograms.

Quantitative PCR (qPCR)—RNA was extracted from cells using the Monarch Total RNA Miniprep Kit (New England Biolabs, T2010S) according to manufacturer's instructions. Synthesis of cDNA from 100 ng input RNA was performed using the iScript RT Supermix for RT-qPCR (Bio-Rad Laboratories, 1708840). Primers were predesigned (PrimeTime qPCR Primers, Integrated DNA Technologies) and can be found in Table S2. SsoAdvanced Universal SYBR Green Supermix (Bio-Rad Laboratories, 1725271) was used in the PCR reaction. qPCR was performed on the CFX96 Touch Real-Time PCR Detection System (Bio-Rad Laboratories) using the following 3-step amplification protocol: 1× 95 °C (30 sec); 40× 95 °C (10 sec), 60 °C (30 sec); Plate Read. Fold changes in mRNA levels were determined using the 2-delta cycle threshold method, normalized to RPLP0 mRNA.

siRNA transfections—Huh7 siRNA transfections were performed according to manufacturer's instructions using 30 μM siRNA and DharmaFECT 4 Transfection Reagent (Horizon, T-2004-02). Negative control siRNAs were from Qiagen (#1022076), SQLE siRNAs from Horizon (#L-009646-00-0005, ON-TARGETplus Human SQLE (6713) siRNA

- SMARTpool), and SCD1 siRNAs from Horizon (#L-005061-00-0005, ON-TARGETplus Human SCD (6319) siRNA - SMARTpool).

Genome-Wide Huh7 CRISPR-Cas9 Screens—Genome-wide CRISPR-Cas9 screens were performed using the Bassik Human CRISPR Knockout Library[28]. The library consists of nine sublibraries, comprising a total of 225,171 elements, including 212,821 sgRNAs targeting 20,549 genes (~10 sgRNAs per gene) and 12,350 negative-control sgRNAs. To generate lentiviral particles, each sublibrary was co-transfected with third-generation lentiviral packaging plasmids into HEK293T cells. Media containing lentivirus was collected 48 and 72 hr after transfection, combined, and filtered. Huh7 PLIN2-GFP cells stably expressing Cas9 were transduced with lentiviral packaged sublibraries (one sublibrary at a time) in 8 μg/ml polybrene. After 72 hr of growth, infected cells were selected in media containing 2 μg/ml puromycin until over 90% of cells were mCherry positive (via flow cytometry). Cells were then recovered for 3–5 days in media lacking puromycin and frozen in liquid nitrogen.

For the screen, library infected cells were thawed (one sublibrary at a time) and expanded at 1000x coverage (1,000 cells per library element). For the steady state genome-wide screen, cells were seeded into 500-cm2 plates (about 10^6 cells per plate, total number of cells seeded was at least 1,000-fold library coverage). For the lipolysis screen, cells were seeded into 500-cm2 plates (about 5 × 10^6 cells per plate). The next day, cells were treated with 1 μg/ml triacsin C for 24 hr. On the day of the sort, cells were dissociated using 0.25% Trypsin-EDTA (Gibco), collected by centrifugation at 300× g for 3 min, and washed 1x with DPBS. Cells were resuspended in phenol red free media (HyClone, 16777-406) supplemented with 3% FBS and 1% BSA (fatty acid free) and kept on ice until FACS.

For both screens, cells were sorted on a BD Aria Fusion equipped with 4 Lasers (488nm, 405nm, 561nm, and 640nm). The brightest 30% GFP^+ and dimmest 30% GFP^+, $mCherry^+$ populations were sorted into 15 ml conicals containing DMEM with 4.5 g/l glucose and l-glutamine (Corning) supplemented with 10% FBS. For each sublibrary sort, at least 1000x as many cells as guides were collected. Sorted cells were collected by centrifugation at 1,000× g for 10 min, washed 1x with DPBS, and pellets frozen at −80 °C until genomic DNA extractions.

Genomic DNA was extracted using the QIAamp DNA Blood Midi Kit (Qiagen) according to the manufacturer's instructions. Guide sequence libraries were prepared from genomic DNA by two rounds of PCR using Herculase II Fusion DNA Polymerase (Agilent, 600679). First, guide sequences were amplified from genomic DNA in the following reaction (per 100 μl reaction): 10 μg genomic DNA, 5x Herculase buffer (20 μl), 100 μM oMCB_1562 (1 μl), 100 μM oMCB_1563 (1 μl), 100 mM dNTPs (1 μl), Herculase II Fusion DNA Polymerase (2 μl), and nuclease-free water (to 100 μl). PCR conditions were as follows: 1× 98 °C (2 min); 18× 98 °C (30 sec), 59.1 °C (30 sec), 72° C (45 sec); 1× 72 °C (3 min).

Amplicons were indexed using Illumina TruSeq LT adapter sequences (for downstream deep sequencing analysis) as described in Morgens et al.[28] and Mathiowetz et al.[68] in the following reaction (per 100 μl reaction): 5 μl PCR1 reaction, 5x Herculase buffer (20 μl),

100 μM oMCB_1439 (0.8 μl), 100 μM barcoded oMCB_1440 (0.8 μl), 100 mM dNTPs (2 μl), Herculase II Fusion DNA Polymerase (2 μl), and nuclease-free water (to 100 μl). PCR conditions were as follows: 1× 98 °C (2 min); 20× 98 °C (30 sec), 59.1 °C (30 sec), 72 °C (45 sec); 1× 72 °C (3 min).

PCR products were separated on a 2% tris-borate-EDTA (TBE)-agarose gel, purified using the QIAquick Gel Extraction Kit (Qiagen, 28704) and assessed for quality using a Fragment Analyzer (Agilent). PCR amplicons from each sublibrary-pair (GFP^{high} and GFP^{low}) were pooled based on sample concentrations (as determined by Qubit Fluorometric Quantification) and the number of elements in each sublibrary. sgRNA sequences were analyzed by deep sequencing using the standard Illumina indexing primer and the custom sequencing primer oMCB_1672 (see Mathiowetz et al[68]) on an Illumina NextSeq instrument at the Oklahoma Medical Research Foundation (https://omrf.org/).

Sequence reads were aligned to the sgRNA reference library using Bowtie 2 software. For each gene, a gene effect and score (likely maximum effect size and score) and *p*-values were calculated using the Cas9 high-Throughput maximum Likelihood Estimator (casTLE) statistical framework as previously described[27]. Deep sequencing counts from the genome-wide screens in PLIN2-GFP reporter cells are available in supplemental tables (Tables S3,S4).

Construction of the custom "Human Lipid Droplet and Metabolism" sgRNA Library—The custom Human Lipid Droplet and Metabolism Library (Addgene, 191535) contains 13,920 elements, with 11,920 sgRNAs targeting 1,196 genes (~10 sgRNAs per gene) and 2,000 negative control sgRNAs. Guide sequences were from the Bassik Human CRISPR Knockout Library[28], and the library construction protocol was previously described[27,28].

Briefly, oligonucleotides were synthesized by Twist Biosciences and consist of the guide sequence flanked by BstXI and BlpI restriction enzyme sites and PCR primer sites. The lyophilized oligo pool was resuspended in Tris-HCl (pH 8) and PCR-amplified using KAPA HiFi HotStart DNA Polymerase (Roche, KK2502) with 52 °C anneal and 15 sec extension (10 cycles). PCR products were pooled and purified over a Qiagen MinElute PCR Purification Kit column (Qiagen, 28004) according to manufacturer's instructions. Eluted samples were restriction digested with BstXI/BlpI overnight at 37 °C. Insert samples were run on a 20% native PAGE gel (Novex TBE Gels, Thermo Fisher Scientific, EC63155BOX), and the band (33 bp) was excised and purified over a Costar Spin X column (Corning, CLS8160). Insert was isopropanol precipitated and resuspended in Qiagen EB. Library vector (pMCB320; Addgene, 89359) was restriction digested with BstXI/BlpI for 1 hr at 37 °C, followed by gel purification with the QIAquick Gel Extraction Kit (Qiagen, 28704). Insert DNA was ligated to digested vector (50 ng digested vector: 1 ng digested insert) for 16 hr at 16 °C.

Ligation products were transformed into Lucigen Endura Electrocompetent Cells (Lucigen, 60242) using a Gene Pulser II (Bio-Rad Laboratories) according to manufacturer's instructions using the following electroporation conditions: 1.8 kV, 600 Ω, 10 μF. Cells were

recovered for 2 hr at 37 °C, plated on 500-cm2 agar plates with 100 μg/ml carbenicillin, and grown overnight at 37 °C. The next day, colonies were scraped off plates and library plasmids purified using a Qiagen HiSpeed Maxi kit (Qiagen, 12662). Plasmids were eluted in Qiagen Buffer TE, aliquoted, and stored at −80 °C.

For deep sequencing, library plasmids were amplified and indexed using Illumina TruSeq LT adapter sequences using Herculase II Fusion DNA Polymerase (Agilent, 600679) as described in Morgens et al.[28] and Mathiowetz et al.[68] in the following reaction (per 100 μl reaction): ~10 ng purified library plasmid pool, 5x Herculase buffer (20 μl), 100 μM oMCB_1439 (0.8 μl), 100 μM barcoded oMCB_1440 (0.8 μl), 100 mM dNTPs (2 μl), Herculase II Fusion DNA Polymerase (2 μl), and nuclease-free water (to 100 μl). PCR conditions were as follows: 1× 98 °C (2 min); 20× 98 °C (30 sec), 59.1 °C (30 sec), 72 °C (45 sec); 1× 72 °C (3 min).

PCR products were separated on a 2% tris-borate-EDTA (TBE)-agarose gel, purified using the QIAquick Gel Extraction Kit (Qiagen, 28704), and assessed for quality using a Fragment Analyzer (Agilent). PCR amplicons were sequenced using the standard Illumina indexing primer and the custom sequencing primer oMCB1672 on an Illumina MiSeq instrument at the Oklahoma Medical Research Foundation. Sequence reads were aligned to the custom Human Lipid Droplet and Metabolism sgRNA reference library using Bowtie 2 software, and library element distribution was assessed using the casTLE plotDist.py script[27]. A list of genes and guides from the Lipid Droplet and Metabolism library is available in Supplementary Table S2.

Lipid Droplet and Metabolism Library CRISPR-Cas9 screens—Huh7 PLIN2-GFP, Huh7 PLIN2-GFP-P2A-BFP, HepG2 PLIN2-GFP, and 786-O PLIN2-GFP cells were screened with our custom Human Lipid Droplet and Metabolism Library (Addgene, 191535). The library consists of 13,920 elements, including 11,920 sgRNAs targeting 1,196 genes (~10 sgRNAs per gene) and 2,000 negative-control sgRNAs. To generate lentiviral particles, each sublibrary was co-transfected with third-generation lentiviral packaging plasmids into HEK293T cells. Media containing lentivirus was collected 48 and 72 hr after transfection, combined, and filtered. Huh7 PLIN2-GFP, Huh7 PLIN2-GFP-P2A-BFP, HepG2 PLIN2-GFP, and 786-O PLIN2-GFP cells stably expressing Cas9 were transduced with the lentiviral packaged library with polybrene (8 μg/ml for Huh7; 2 μg/ml for HepG2; 1 μg/ml for 786-O). After 72 hr of growth, infected cells were selected in media containing puromycin (2 μg/ml for all cell lines) until over 90% of cells were mCherry positive (via flow cytometry). Cells were then recovered for 3–5 days (Huh7) or 5–7 days (HepG2, 786-O) in media lacking puromycin and frozen in liquid nitrogen.

For each screen, cells were thawed and expanded at >1000x coverage. For all screens, cells were seeded into 500-cm2 plates at 1,000-fold library coverage. For the Huh7 lipolysis screen, cells were treated the following day with 1 μg/ml triacsin C for 24 hr. For the 786-O oleate screen, cells were treated with 100 μM oleate-BSA complex for 24 hr. For all screens, on the day of the sort, cells were dissociated using 0.25% Trypsin-EDTA (Gibco), collected by centrifugation at 300× g for 3 min, and washed 1x with DPBS. Cells were resuspended

in phenol red free media (HyClone, 16777-406) supplemented with 3% FBS and 1% BSA (fatty acid free) and kept on ice until FACS.

Cells were sorted on a BD FACSAria Fusion equipped with 4 Lasers (488 nm, 405 nm, 561 nm, and 640 nm). sgRNA-expressing, mCherry$^+$ cells were sorted as follows: GFP screens (brightest 30% GFP$^+$ and dimmest 30% GFP$^+$), BFP screens (brightest 30% BFP$^+$ and dimmest 30% BFP$^+$), GFP:BFP screens (brightest 30% GFP:BFP ratio and dimmest 30% GFP:BFP ratio). Cells were sorted into 15 ml conicals containing DMEM with 4.5 g/L glucose and L-glutamine supplemented with 10% FBS. For each sort, at least ~14 ×10^6 cells were collected (at least 1,000x coverage). Sorted cells were collected by centrifugation at 1,000× g for 10 min, washed 1x with DPBS, and pellets frozen at −80 °C until genomic DNA extractions.

Genomic DNA was extracted, guide sequences PCR amplified and indexed, and guide enrichment analyzed using casTLE as described above ("Genome-Wide Huh7 CRISPR-Cas9 Screens"). Deep sequencing counts from each Lipid Droplet & Metabolism Library screen are available in Supplemental Tables S5–S8.

Lipidomics

Chemicals: Materials used for liquid chromatography/mass spectrometry were: water (Optima® LC/MS grade, Fisher Chemical, W6–4), acetonitrile (Optima® LC/MS grade, Fisher Chemical, A955-4), 2-propanol (hypergrade for LC-MS, Supelco, 1.02781.4000), ammonium formate (Lichropur for LC-MS, Sigma-Aldrich, 70221-25G-F) and formic acid (Optima® LC/MS grade, Fisher Chemical, A117-50).

Solvents for lipid extraction were tert-butyl methyl ether (HPLC grade, Sigma-Aldrich, 34875-1L) and methanol (HPLC grade, Fisher Scientific, A452-4) that were spiked with 0.1% (w/v) 2,6-Di-tert-butyl-4-methylphenol (GC grade, Sigma-Aldrich, B1378-100G).

Lipid internal standard mixture was SPLASH ® LIPIDOMIX ® Mass Spec Standard (Avanti Polar Lipids, 330707-1EA).

Sample preparation: Approximately 2 million cells were scraped and washed 2x with cold DPBS. Cells were pelleted at 500 ×g for 5 min, supernatant was removed, and cell pellets were stored at −80C until extraction. Before extraction, cell pellets were thawed on ice for 30 min and resuspended in 50 µl PBS. Internal standards (5 µl SPLASH® LIPIDOMIX® per sample) dissolved in methanol were added directly to each suspension. Lipids were extracted by adding tert-butyl methyl ether (1250 µl) and methanol (375 µL). The mixture was incubated on an orbital mixer for 1 hr (room temperature, 32 rpm). To induce phase separation, water (315 µL) was added, and the mixture was incubated on an orbital mixer for 10 min (room temperature, 32 rpm). Samples were centrifuged (room temperature, 10 min, 17,000 × g). Upper organic phase with collected and subsequently dried in vacuo (Eppendorf concentrator 5301, 1 ppm).

Liquid Chromatography: Dried lipid extracts were reconstituted in chloroform/methanol (150 µl, 2:1, v/v) and 15 µl of each extract was transferred to HPLC vials containing glass

inserts. Quality control samples were generated by mixing equal volumes of each lipid extract followed by aliquotation in 15 µl aliquots. Aliquoted extracts were dried in vacuo (Eppendorf concentrator 5301, 1 ppm) and redissolved in 2-propanol (15 µl) for injection.

Lipids were separated by reversed phase liquid chromatography on a Vanquish Core (Thermo Fisher Scientific, Bremen, Germany) equipped with an Accucore C30 column (150 × 2.1 mm; 2.6 µm, 150 Å, Thermo Fisher Scientific, Bremen, Germany). Lipids were separated by gradient elution with solvent A (acetonitrile/water, 1:1, v/v) and B (2-propanol/acetonitrile/water, 85:10:5, v/v) both containing 5 mM ammonium formate and 0.1% (v/v) formic acid. Separation was performed at 50°C with a flow rate of 0.3 mL/min using the following gradient: 0–15 min – 25 to 86 % B (curve 5), 15–21 min – 86 to 100 % B (curve 5), 21–34.5 min – 100 % B isocratic, 34.5–34.6 min – 100 to 25 % B (curve 5), followed by 8 min re-equilibration at 25 % B.

Mass Spectrometry: Reversed phase liquid chromatography was coupled on-line to a Q Exactive Plus Hybrid Quadrupole Orbitrap mass spectrometer (Thermo Fisher Scientific, Bremen, Germany) equipped with a HESI probe. Mass spectra were acquired in positive mode with the following ESI parameters: sheath gas – 40 L/min, auxiliary gas – 10 L/min, sweep gas – 1 L/min, spray voltage – 3.5 kV (positive ion mode); capillary temperature – 250 °C, S-lens RF level – 35 and aux gas heater temperature – 370 °C.

Data acquisition for lipid identification was performed in quality control samples by acquiring data in data dependent acquisition mode (DDA). DDA parameters featured a survey scan resolution of 140,000 (at m/z 200), AGC target 1e6 Maximum injection time 100 ms in a scan range of m/z 240–1200. Data dependent MS/MS scans were acquired with a resolution of 17,500, AGC target 1e5, Maximum injection time 60 ms, loop count 15, isolation window 1.2 m/z and stepped normalized collision energies of 10, 20 and 30 %. A data dependent MS2 was triggered when an AGC target of 2e2 was reached followed by a Dynamic Exclusion for 10 s. All isotopes and charge states > 1 were excluded. All data was acquired in profile mode.

For deep lipidome profiling, iterative exclusion was performed using the IE omics R package[70]. This package generates a list for already fragmented precursors from a prior DDA run that can be excluded from subsequent DDA runs ensuring a higher number of unique MS/MS spectra for deep lipidome profiling. After the initial DDA analysis of a quality control sample, another quality control sample was measured but excluding all previously fragmentated precursor ions. Parameters for generating exclusion lists from previous runs were – RT window = 0.3; noiseCount = 15; MZWindow = 0.02 and MaxRT = 36 min. This workflow was repeated one more time to get a total of three consecutive DDA analyses of a quality control sample in positive ionization mode.

Data for lipid quantification was acquired in Full MS mode with following parameters – scan resolution of 140,000 (at m/z 200), AGC target 1e6 Maximum injection time 100 ms in a scan range of m/z 240–1200.

Lipid Identification and Quantification: Lipostar (version 2.1.0, Molecular Discovery, Hertfordshire, UK) equipped with in house generated structure database featuring fatty acids with no information on double bond regio- or stereoisomerism covering glycerolipid, glycerophospholipid, sphingolipid and sterol ester lipid classes. The raw files were imported directly with a Sample MS Signal Filter Signal Threshold = 1000 for MS and a Sample MS/MS Signal Filter Signal Threshold = 10. Automatic peak picking was performed with an m/z tolerance = 5 ppm, chromatography filtering threshold = 0.97, MS filtering threshold = 0.97, Signal filtering threshold = 0. Peaks smoothing was performed using the Savitzky-Golay smoothing algorithm with a window size = 3, degree = 2 and multi-pass iterations = 3. Isotopes were clustered using a m/z tolerance = 5 ppm, RT tolerance = 0.25 min, abundance Dev = 40%, max charge = 1. Peak alignment between samples using an m/z tolerance = 5 ppm and an RT tolerance = 0.25 min. A gap filler with an RT tolerance = 0.05 min and a signal filtering threshold = 0 with an anti Spike filter was applied.

For lipid identification, a “MS/MS only” filter was applied to keep only features with MS/MS spectra for identification. Triacylgylcerols, diacylglycerols and sterol esters were identified as [M+NH4]+ adducts. All phospholipids were identified as [M+H]+ adducts. Following parameters were used for lipid identification: 5 ppm precursor ion mass tolerance and 20 ppm product ion mass tolerance. Automatic approval was performed to keep structures with quality of 3–4 stars. Identifications were refined using manual curation and Kendrick mass defect analysis and lipids that were not following these retention time rules were excluded as false positives.

Quantification by integration of the extracted ion chromatograms of single lipid adducts of these high confidence lipid identifications was manually curated and adjusted. Identified lipids were normalized to peak areas of added internal standards to decrease analytical variation.

For data representation, data was log10 transformed and autoscaled using metaboanalyst.ca[71].

BODIPY 558/568 C12 Incorporation Assays

C12 incubation: For BODIPY C12 TAG biogenesis and lipolysis assays, Huh7 Cas9 control and MARCH6^{KO} cells were seeded in 60-mm plates at 350K cells per plate. For the biogenesis assay (measuring formation of esterified C12), cells were incubated in BODIPY C12-BSA complex (complete media + 1% BSA + 1 μM BODIPY 558/568 C12) for 0, 1, 3, or 6 hr. For the harvest, cells were washed twice, collected in cold DPBS, and transferred to Eppendorf tubes (Eppendorf, 022363352). Cells were centrifuged at 500× g for 5 min, washed in DPBS, and centrifuged again. Cell pellets were stored at −80 °C until the lipid extraction step. For the lipolysis assay (measuring loss of esterified C12), cells were incubated in BODIPY C12-BSA complex for 16 hr. Cells were then washed 3x with media and incubated in fresh media for 1 hr. Cells were then treated with 1 mg/ml triacsin C for 0, 6, 12 or 24 hr. Cells were harvested and pellets stored at −80 °C as described above.

Lipid extractions: Cell pellets were thawed at room temperature and resuspended in 50 μL DPBS. Lipids were extracted by adding tert-butyl methyl ether (1250 μL) and methanol

(375 μL). The mixture was incubated on an orbital mixer for 1 hr at room temperature. To induce phase separation, water (315 μL) was added, and the mixture was incubated on an orbital mixer for 10 min at room temperature. Samples were centrifuged at 1,000× g for 10 minutes at room temperature. The upper organic phase with collected and subsequently dried *in vacuo*.

Thin Layer Chromatography (TLC): Dried lipid extracts were reconstituted in 25 μL chloroform/methanol (2:1, v/v). Lipids were then separated using HPTLC Silica gel 60 F_{254} plates (Sigma, 1137270001). Briefly, the samples (10 μL each) were spotted onto TLC plates and developed in $CHCl_3$/EtOH/TEA/H_2O (5:5:5:1, v/v). For imaging BODIPY C12 fluorescence, plates were imaged on a ChemiDoc MP Imaging System (Bio-Rad Laboratories). Band densitometry analysis was performed using Image Lab 5.0 (Bio-Rad Laboratories). The reported mean ± standard deviation was determined from three biological replicates.

Quantification and Statistical Analysis—All statistical analyses were performed using Prism 9 (GraphPad). For each panel, the number of biological replicates (n), *p*-values, and statistical tests employed are reported in figure legends and methods.

Supplementary Material

Refer to Web version on PubMed Central for supplementary material.

ACKNOWLEDGEMENTS

This research was supported by grants from the National Institutes of Health (R01GM112948 and R01DK128099 to J.A.O., F31DK121477 to M.A.R., F32GM113370 to D.E.L., R01GM074874 to R.R.K.) and from the Chan Zuckerberg Initiative Neurodegeneration Challenge Network to M.K. J.A.O. and M.K. are Chan Zuckerberg Biohub Investigators. D.E.L. was also supported by an Alpha-1 Foundation postdoctoral fellowship. F.F. and M.A.N were supported in part by the Intramural Research Programs of the National Institute on Aging (NIA) part of the National Institutes of Health, Department of Health and Human Services; project number Z01-AG000535-014. E.E. was supported by a Cayman Biomedical Research Institute (CABRI) Undergraduate Fellowship.

REFERENCES

1. Olzmann JA, and Carvalho P (2019). Dynamics and functions of lipid droplets. Nat Rev Mol Cell Biol 20, 137–155. 10.1038/s41580-018-0085-z. [PubMed: 30523332]
2. Walther TC, Chung J, and Farese RV (2017). Lipid Droplet Biogenesis. Annu Rev Cell Dev Biol 33, 491–510. 10.1146/annurev-cellbio-100616-060608. [PubMed: 28793795]
3. Renne MF, Klug YA, and Carvalho P (2020). Lipid droplet biogenesis: A mystery “unmixing”? Semin Cell Dev Biol 108, 14–23. 10.1016/j.semcdb.2020.03.001. [PubMed: 32192830]
4. Thiam AR, and Ikonen E (2021). Lipid Droplet Nucleation. Trends Cell Biol 31, 108–118. 10.1016/j.tcb.2020.11.006. [PubMed: 33293168]
5. Bersuker K, and Olzmann JA (2017). Establishing the lipid droplet proteome: Mechanisms of lipid droplet protein targeting and degradation. Biochim Biophys Acta Mol Cell Biol Lipids 1862, 1166–1177. 10.1016/j.bbalip.2017.06.006. [PubMed: 28627435]
6. Krahmer N, Hilger M, Kory N, Wilfling F, Stoehr G, Mann M, Farese RV, and Walther TC (2013). Protein correlation profiles identify lipid droplet proteins with high confidence. Mol Cell Proteomics 12, 1115–1126. 10.1074/mcp.M112.020230. [PubMed: 23319140]

7. Liu P, Ying Y, Zhao Y, Mundy DI, Zhu M, and Anderson RGW (2004). Chinese hamster ovary K2 cell lipid droplets appear to be metabolic organelles involved in membrane traffic. J Biol Chem 279, 3787–3792. 10.1074/jbc.M311945200. [PubMed: 14597625]
8. Roberts MA, and Olzmann JA (2020). Protein quality control and lipid droplet metabolism. Annu Rev Cell Dev Biol 36, 115–139. 10.1146/annurev-cellbio-031320-101827. [PubMed: 33021827]
9. Kimmel AR, and Sztalryd C (2016). The Perilipins: Major Cytosolic Lipid Droplet-Associated Proteins and Their Roles in Cellular Lipid Storage, Mobilization, and Systemic Homeostasis. Annu Rev Nutr 36, 471–509. 10.1146/annurev-nutr-071813-105410. [PubMed: 27431369]
10. Najt CP, Devarajan M, and Mashek DG (2022). Perilipins at a glance. Journal of Cell Science 135, jcs259501. 10.1242/jcs.259501. [PubMed: 35260890]
11. Orlicky DJ, Libby AE, Bales ES, McMahan RH, Monks J, La Rosa FG, and McManaman JL (2019). Perilipin-2 promotes obesity and progressive fatty liver disease in mice through mechanistically distinct hepatocyte and extra-hepatocyte actions. J Physiol (Lond) 597, 1565–1584. 10.1113/JP277140. [PubMed: 30536914]
12. Griffin JD, Bejarano E, Wang X-D, and Greenberg AS (2021). Integrated Action of Autophagy and Adipose Tissue Triglyceride Lipase Ameliorates Diet-Induced Hepatic Steatosis in Liver-Specific PLIN2 Knockout Mice. Cells 10, 1016. 10.3390/cells10051016. [PubMed: 33923083]
13. Najt CP, Senthivinayagam S, Aljazi MB, Fader KA, Olenic SD, Brock JRL, Lydic TA, Jones AD, and Atshaves BP (2016). Liver-specific loss of Perilipin 2 alleviates diet-induced hepatic steatosis, inflammation, and fibrosis. Am J Physiol Gastrointest Liver Physiol 310, G726–38. 10.1152/ajpgi.00436.2015. [PubMed: 26968211]
14. Listenberger LL, Ostermeyer-Fay AG, Goldberg EB, Brown WJ, and Brown DA (2007). Adipocyte differentiation-related protein reduces the lipid droplet association of adipose triglyceride lipase and slows triacylglycerol turnover. J Lipid Res 48, 2751–2761. 10.1194/jlr.M700359-JLR200. [PubMed: 17872589]
15. Faulkner CS, White CM, Shah VH, and Jophlin LL (2020). A single nucleotide polymorphism of PLIN2 is associated with nonalcoholic steatohepatitis and causes phenotypic changes in hepatocyte lipid droplets: A pilot study. Biochim Biophys Acta Mol Cell Biol Lipids 1865, 158637. 10.1016/j.bbalip.2020.158637. [PubMed: 31981756]
16. Magné J, Aminoff A, Perman Sundelin J, Mannila MN, Gustafsson P, Hultenby K, Wernerson A, Bauer G, Listenberger L, Neville MJ, et al. (2013). The minor allele of the missense polymorphism Ser251Pro in perilipin 2 (PLIN2) disrupts an α-helix, affects lipolysis, and is associated with reduced plasma triglyceride concentration in humans. FASEB J 27, 3090–3099. 10.1096/fj.13-228759. [PubMed: 23603836]
17. Sentinelli F, Capoccia D, Incani M, Bertoccini L, Severino A, Pani MG, Manconi E, Cossu E, Leonetti F, and Baroni MG (2016). The perilipin 2 (PLIN2) gene Ser251Pro missense mutation is associated with reduced insulin secretion and increased insulin sensitivity in Italian obese subjects. Diabetes/Metabolism Research and Reviews 32, 550–556. 10.1002/dmrr.2751. [PubMed: 26443937]
18. Gluchowski NL, Becuwe M, Walther TC, and Farese RV (2017). Lipid droplets and liver disease: from basic biology to clinical implications. Nat Rev Gastroenterol Hepatol 14, 343–355. 10.1038/nrgastro.2017.32. [PubMed: 28428634]
19. Straub BK, Stoeffel P, Heid H, Zimbelmann R, and Schirmacher P (2008). Differential pattern of lipid droplet-associated proteins and de novo perilipin expression in hepatocyte steatogenesis. Hepatology 47, 1936–1946. 10.1002/hep.22268. [PubMed: 18393390]
20. Marschallinger J, Iram T, Zardeneta M, Lee SE, Lehallier B, Haney MS, Pluvinage JV, Mathur V, Hahn O, Morgens DW, et al. (2020). Lipid-droplet-accumulating microglia represent a dysfunctional and proinflammatory state in the aging brain. Nat Neurosci 23, 194–208. 10.1038/s41593-019-0566-1. [PubMed: 31959936]
21. Cruz ALS, Barreto E. de A., Fazolini NPB, Viola JPB, and Bozza PT (2020). Lipid droplets: platforms with multiple functions in cancer hallmarks. Cell Death Dis 11, 105. 10.1038/s41419-020-2297-3. [PubMed: 32029741]
22. Xu S, Zou F, Diao Z, Zhang S, Deng Y, Zhu X, Cui L, Yu J, Zhang Z, Bamigbade AT, et al. (2019). Perilipin 2 and lipid droplets provide reciprocal stabilization. Biophys Rep 5, 145–160. 10.1007/s41048-019-0091-5.

23. Kaushik S, and Cuervo AM (2015). Degradation of lipid droplet-associated proteins by chaperone-mediated autophagy facilitates lipolysis. Nat Cell Biol 17, 759–770. 10.1038/ncb3166. [PubMed: 25961502]
24. Masuda Y, Itabe H, Odaki M, Hama K, Fujimoto Y, Mori M, Sasabe N, Aoki J, Arai H, and Takano T (2006). ADRP/adipophilin is degraded through the proteasome-dependent pathway during regression of lipid-storing cells. J Lipid Res 47, 87–98. 10.1194/jlr.M500170-JLR200. [PubMed: 16230742]
25. Nguyen KT, Lee C-S, Mun S-H, Truong NT, Park SK, and Hwang C-S (2019). N-terminal acetylation and the N-end rule pathway control degradation of the lipid droplet protein PLIN2. J Biol Chem 294, 379–388. 10.1074/jbc.RA118.005556. [PubMed: 30425097]
26. Xu G, Sztalryd C, Lu X, Tansey J, Gan J, Dorward H, Kimmel A, and Londos C (2005). Post-translational regulation of adipose differentiation-related protein by the ubiquitin/proteasome pathway. J Biol Chem 280, 42841–42847. 10.1074/jbc.M506569200. [PubMed: 16115879]
27. Morgens DW, Deans RM, Li A, and Bassik MC (2016). Systematic comparison of CRISPR/Cas9 and RNAi screens for essential genes. Nat Biotechnol 34, 634–636. 10.1038/nbt.3567. [PubMed: 27159373]
28. Morgens DW, Wainberg M, Boyle EA, Ursu O, Araya CL, Tsui CK, Haney MS, Hess GT, Han K, Jeng EE, et al. (2017). Genome-scale measurement of off-target activity using Cas9 toxicity in high-throughput screens. Nat Commun 8, 15178. 10.1038/ncomms15178. [PubMed: 28474669]
29. Bassik MC, Kampmann M, Lebbink RJ, Wang S, Hein MY, Poser I, Weibezahn J, Horlbeck MA, Chen S, Mann M, et al. (2013). A systematic mammalian genetic interaction map reveals pathways underlying ricin susceptibility. Cell 152, 909–922. 10.1016/j.cell.2013.01.030. [PubMed: 23394947]
30. Dubreuil MM, Morgens DW, Okumoto K, Honsho M, Contrepois K, Lee-McMullen B, Traber GM, Sood RS, Dixon SJ, Snyder MP, et al. (2020). Systematic Identification of Regulators of Oxidative Stress Reveals Non-canonical Roles for Peroxisomal Import and the Pentose Phosphate Pathway. Cell Rep 30, 1417–1433.e7. 10.1016/j.celrep.2020.01.013. [PubMed: 32023459]
31. Han K, Jeng EE, Hess GT, Morgens DW, Li A, and Bassik MC (2017). Synergistic drug combinations for cancer identified in a CRISPR screen for pairwise genetic interactions. Nat Biotechnol 35, 463–474. 10.1038/nbt.3834. [PubMed: 28319085]
32. Parnas O, Jovanovic M, Eisenhaure TM, Herbst RH, Dixit A, Ye CJ, Przybylski D, Platt RJ, Tirosh I, Sanjana NE, et al. (2015). A Genome-wide CRISPR Screen in Primary Immune Cells to Dissect Regulatory Networks. Cell 162, 675–686. 10.1016/j.cell.2015.06.059. [PubMed: 26189680]
33. Bersuker K, Peterson CWH, To M, Sahl SJ, Savikhin V, Grossman EA, Nomura DK, and Olzmann JA (2018). A Proximity Labeling Strategy Provides Insights into the Composition and Dynamics of Lipid Droplet Proteomes. Dev Cell 44, 97–112.e7. 10.1016/j.devcel.2017.11.020. [PubMed: 29275994]
34. Bailey AP, Koster G, Guillermier C, Hirst EMA, MacRae JI, Lechene CP, Postle AD, and Gould AP (2015). Antioxidant role for lipid droplets in a stem cell niche of drosophila. Cell 163, 340–353. 10.1016/j.cell.2015.09.020. [PubMed: 26451484]
35. Jin Y, Tan Y, Chen L, Liu Y, and Ren Z (2018). Reactive Oxygen Species Induces Lipid Droplet Accumulation in HepG2 Cells by Increasing Perilipin 2 Expression. IJMS 19, 3445. 10.3390/ijms19113445. [PubMed: 30400205]
36. Liu L, MacKenzie KR, Putluri N, Maletić-Savatić M, and Bellen HJ (2017). The Glia-Neuron Lactate Shuttle and Elevated ROS Promote Lipid Synthesis in Neurons and Lipid Droplet Accumulation in Glia via APOE/D. Cell Metab 26, 719–737.e6. 10.1016/j.cmet.2017.08.024. [PubMed: 28965825]
37. Nowinski SM, Solmonson A, Rusin SF, Maschek JA, Bensard CL, Fogarty S, Jeong M-Y, Lettlova S, Berg JA, Morgan JT, et al. (2020). Mitochondrial fatty acid synthesis coordinates oxidative metabolism in mammalian mitochondria. eLife 9, e58041. 10.7554/eLife.58041. [PubMed: 32804083]
38. Kaushik S, and Cuervo AM (2016). AMPK-dependent phosphorylation of lipid droplet protein PLIN2 triggers its degradation by CMA. Autophagy 12, 432–438. 10.1080/15548627.2015.1124226. [PubMed: 26902588]

39. Foresti O, Ruggiano A, Hannibal-Bach HK, Ejsing CS, and Carvalho P (2013). Sterol homeostasis requires regulated degradation of squalene monooxygenase by the ubiquitin ligase Doa10/Teb4. eLife 2, e00953. 10.7554/eLife.00953. [PubMed: 23898401]
40. Gill S, Stevenson J, Kristiana I, and Brown AJ (2011). Cholesterol-dependent degradation of squalene monooxygenase, a control point in cholesterol synthesis beyond HMG-CoA reductase. Cell Metab 13, 260–273. 10.1016/j.cmet.2011.01.015. [PubMed: 21356516]
41. Stevenson J, Huang EY, and Olzmann JA (2016). Endoplasmic Reticulum-Associated Degradation and Lipid Homeostasis. Annu Rev Nutr 36, 511–542. 10.1146/annurev-nutr-071715-051030. [PubMed: 27296502]
42. Romanauska A, and Köhler A (2018). The Inner Nuclear Membrane Is a Metabolically Active Territory that Generates Nuclear Lipid Droplets. Cell 174, 700–715.e18. 10.1016/j.cell.2018.05.047. [PubMed: 29937227]
43. Ghosh M, Niyogi S, Bhattacharyya M, Adak M, Nayak DK, Chakrabarti S, and Chakrabarti P (2016). Ubiquitin ligase COP1 controls hepatic fat metabolism by targeting ATGL for degradation. Diabetes 65, 3561–3572. 10.2337/db16-0506. [PubMed: 27658392]
44. Olzmann JA, Richter CM, and Kopito RR (2013). Spatial regulation of UBXD8 and p97/VCP controls ATGL-mediated lipid droplet turnover. Proc Natl Acad Sci USA 110, 1345–1350. 10.1073/pnas.1213738110. [PubMed: 23297223]
45. Goo Y-H, Son S-H, and Paul A (2017). Lipid Droplet-Associated Hydrolase Promotes Lipid Droplet Fusion and Enhances ATGL Degradation and Triglyceride Accumulation. Sci Rep 7, 2743. 10.1038/s41598-017-02963-y. [PubMed: 28578400]
46. Patel S, Yang W, Kozusko K, Saudek V, and Savage DB (2014). Perilipins 2 and 3 lack a carboxy-terminal domain present in perilipin 1 involved in sequestering ABHD5 and suppressing basal lipolysis. Proc Natl Acad Sci USA 111, 9163–9168. 10.1073/pnas.1318791111. [PubMed: 24927580]
47. Listenberger LL, Han X, Lewis SE, Cases S, Farese RV, Ory DS, and Schaffer JE (2003). Triglyceride accumulation protects against fatty acid-induced lipotoxicity. Proc Natl Acad Sci USA 100, 3077–3082. 10.1073/pnas.0630588100. [PubMed: 12629214]
48. Rambold AS, Cohen S, and Lippincott-Schwartz J (2015). Fatty acid trafficking in starved cells: regulation by lipid droplet lipolysis, autophagy, and mitochondrial fusion dynamics. Dev Cell 32, 678–692. 10.1016/j.devcel.2015.01.029. [PubMed: 25752962]
49. Huang D, Xu B, Liu L, Wu L, Zhu Y, Ghanbarpour A, Wang Y, Chen F-J, Lyu J, Hu Y, et al. (2021). TMEM41B acts as an ER scramblase required for lipoprotein biogenesis and lipid homeostasis. Cell Metabolism 33, 1655–1670.e8. 10.1016/j.cmet.2021.05.006. [PubMed: 34015269]
50. Li YE, Wang Y, Du X, Zhang T, Mak HY, Hancock SE, McEwen H, Pandzic E, Whan RM, Aw YC, et al. (2021). TMEM41B and VMP1 are scramblases and regulate the distribution of cholesterol and phosphatidylserine. Journal of Cell Biology 220, e202103105. 10.1083/jcb.202103105. [PubMed: 33929485]
51. Moretti F, Bergman P, Dodgson S, Marcellin D, Claerr I, Goodwin JM, DeJesus R, Kang Z, Antczak C, Begue D, et al. TMEM41B is a novel regulator of autophagy and lipid mobilization. EMBO Reports 19. 10.15252/embr.201845889.
52. Sun Z, Miller RA, Patel RT, Chen J, Dhir R, Wang H, Zhang D, Graham MJ, Unterman TG, Shulman GI, et al. (2012). Hepatic Hdac3 promotes gluconeogenesis by repressing lipid synthesis and sequestration. Nat Med 18, 934–942. 10.1038/nm.2744. [PubMed: 22561686]
53. Hayhurst GP, Lee Y-H, Lambert G, Ward JM, and Gonzalez FJ (2001). Hepatocyte Nuclear Factor 4α (Nuclear Receptor 2A1) Is Essential for Maintenance of Hepatic Gene Expression and Lipid Homeostasis. Molecular and Cellular Biology 21, 1393–1403. 10.1128/MCB.21.4.1393-1403.2001. [PubMed: 11158324]
54. Stoffel M, and Duncan SA (1997). The maturity-onset diabetes of the young (MODY1) transcriptionfactor HNF4aregulates expression of genes required for glucosetransport and metabolism. Proceedings of the National Academy of Sciences 94, 13209–13214. 10.1073/pnas.94.24.13209.

55. Tian R, Abarientos A, Hong J, Hashemi SH, Yan R, Dräger N, Leng K, Nalls MA, Singleton AB, Xu K, et al. (2021). Genome-wide CRISPRi/a screens in human neurons link lysosomal failure to ferroptosis. Nat Neurosci 24, 1020–1034. 10.1038/s41593-021-00862-0. [PubMed: 34031600]
56. Bersuker K, Hendricks JM, Li Z, Magtanong L, Ford B, Tang PH, Roberts MA, Tong B, Maimone TJ, Zoncu R, et al. (2019). The CoQ oxidoreductase FSP1 acts parallel to GPX4 to inhibit ferroptosis. Nature 575, 688–692. 10.1038/s41586-019-1705-2. [PubMed: 31634900]
57. Li Z, Ferguson L, Deol KK, Roberts MA, Magtanong L, Hendricks JM, Mousa GA, Kilinc S, Schaefer K, Wells JA, et al. (2022). Ribosome stalling during selenoprotein translation exposes a ferroptosis vulnerability. Nat Chem Biol 18, 751–761. 10.1038/s41589-022-01033-3. [PubMed: 35637349]
58. Zhu XG, Nicholson Puthenveedu S, Shen Y, La K, Ozlu C, Wang T, Klompstra D, Gultekin Y, Chi J, Fidelin J, et al. (2019). CHP1 regulates compartmentalized glycerolipid synthesis by activating GPAT4. Mol Cell 74, 45–58.e7. 10.1016/j.molcel.2019.01.037. [PubMed: 30846317]
59. Lu A, Hsieh F, Sharma BR, Vaughn SR, Enrich C, and Pfeffer SR (2022). CRISPR screens for lipid regulators reveal a role for ER-bound SNX13 in lysosomal cholesterol export. Journal of Cell Biology 221, e202105060. 10.1083/jcb.202105060. [PubMed: 34936700]
60. Morris SNS, Deol KK, Lange M, and Olzmann JA (2022). A genome-wide CRISPR screen implicates plasma membrane asymmetry in exogenous C6-ceramide toxicity. Biology Open 11, bio059695. 10.1242/bio.059695. [PubMed: 36409314]
61. Wang Y, Menon AK, Maki Y, Liu Y-S, Iwasaki Y, Fujita M, Guerrero PA, Silva DV, Seeberger PH, Murakami Y, et al. (2022). Genome-wide CRISPR screen reveals CLPTM1L as a lipid scramblase required for efficient glycosylphosphatidylinositol biosynthesis. Proc. Natl. Acad. Sci. U.S.A. 119, e2115083119. 10.1073/pnas.2115083119. [PubMed: 35344438]
62. Piccolis M, Bond LM, Kampmann M, Pulimeno P, Chitraju C, Jayson CBK, Vaites LP, Boland S, Lai ZW, Gabriel KR, et al. (2019). Probing the global cellular responses to lipotoxicity caused by saturated fatty acids. Mol Cell 74, 32–44.e8. 10.1016/j.molcel.2019.01.036. [PubMed: 30846318]
63. Zhang Y, Lin S, Peng J, Liang X, Yang Q, Bai X, Li Y, Li J, Dong W, Wang Y, et al. (2022). Amelioration of hepatic steatosis by dietary essential amino acid-induced ubiquitination. Mol Cell. 10.1016/j.molcel.2022.01.021.
64. Stefanovic-Barrett S, Dickson AS, Burr SP, Williamson JC, Lobb IT, van den Boomen DJ, Lehner PJ, and Nathan JA (2018). MARCH6 and TRC8 facilitate the quality control of cytosolic and tail-anchored proteins. EMBO Rep 19. 10.15252/embr.201745603.
65. Langmead B, and Salzberg SL (2012). Fast gapped-read alignment with Bowtie 2. Nat Methods 9, 357–359. 10.1038/nmeth.1923. [PubMed: 22388286]
66. Yang H-J, Hsu C-L, Yang J-Y, and Yang WY (2012). Monodansylpentane as a blue-fluorescent lipid-droplet marker for multi-color live-cell imaging. PLoS ONE 7, e32693. 10.1371/journal.pone.0032693. [PubMed: 22396789]
67. Morgens DW, Deans RM, Li A, and Bassik MC (2016). Systematic comparison of CRISPR/Cas9 and RNAi screens for essential genes. Nat Biotechnol 34, 634–636. 10.1038/nbt.3567. [PubMed: 27159373]
68. Mathiowetz AJ, Roberts MA, Morgens DW, Olzmann JA, and Li Z (2023). Protocol for performing pooled CRISPR-Cas9 loss-of-function screens. STAR Protoc 4, 102201. 10.1016/j.xpro.2023.102201. [PubMed: 37000620]
69. Schindelin J, Arganda-Carreras I, Frise E, Kaynig V, Longair M, Pietzsch T, Preibisch S, Rueden C, Saalfeld S, Schmid B, et al. (2012). Fiji: an open-source platform for biological-image analysis. Nat Methods 9, 676–682. 10.1038/nmeth.2019. [PubMed: 22743772]
70. Koelmel JP, Kroeger NM, Gill EL, Ulmer CZ, Bowden JA, Patterson RE, Yost RA, and Garrett TJ (2017). Expanding Lipidome Coverage Using LC-MS/MS Data-Dependent Acquisition with Automated Exclusion List Generation. J Am Soc Mass Spectrom 28, 908–917. 10.1007/s13361-017-1608-0. [PubMed: 28265968]
71. Pang Z, Zhou G, Ewald J, Chang L, Hacariz O, Basu N, and Xia J (2022). Using MetaboAnalyst 5.0 for LC-HRMS spectra processing, multi-omics integration and covariate adjustment of global metabolomics data. Nat Protoc 17, 1735–1761. 10.1038/s41596-022-00710-w. [PubMed: 35715522]

72. Chong J, Wishart DS, and Xia J (2019). Using MetaboAnalyst 4.0 for Comprehensive and Integrative Metabolomics Data Analysis. Current Protocols in Bioinformatics 68, e86. 10.1002/cpbi.86. [PubMed: 31756036]

Highlights

- Generation of genetically edited PLIN2 fluorescent reporter cell lines
- CRISPR screens identify PLIN2 regulators in different cell lines and conditions
- ERAD E3 ligase MARCH6 regulates triacylglycerol biosynthesis and lipid droplets
- Development of CRISPRlipid as a data commons for lipid-related genetic screens

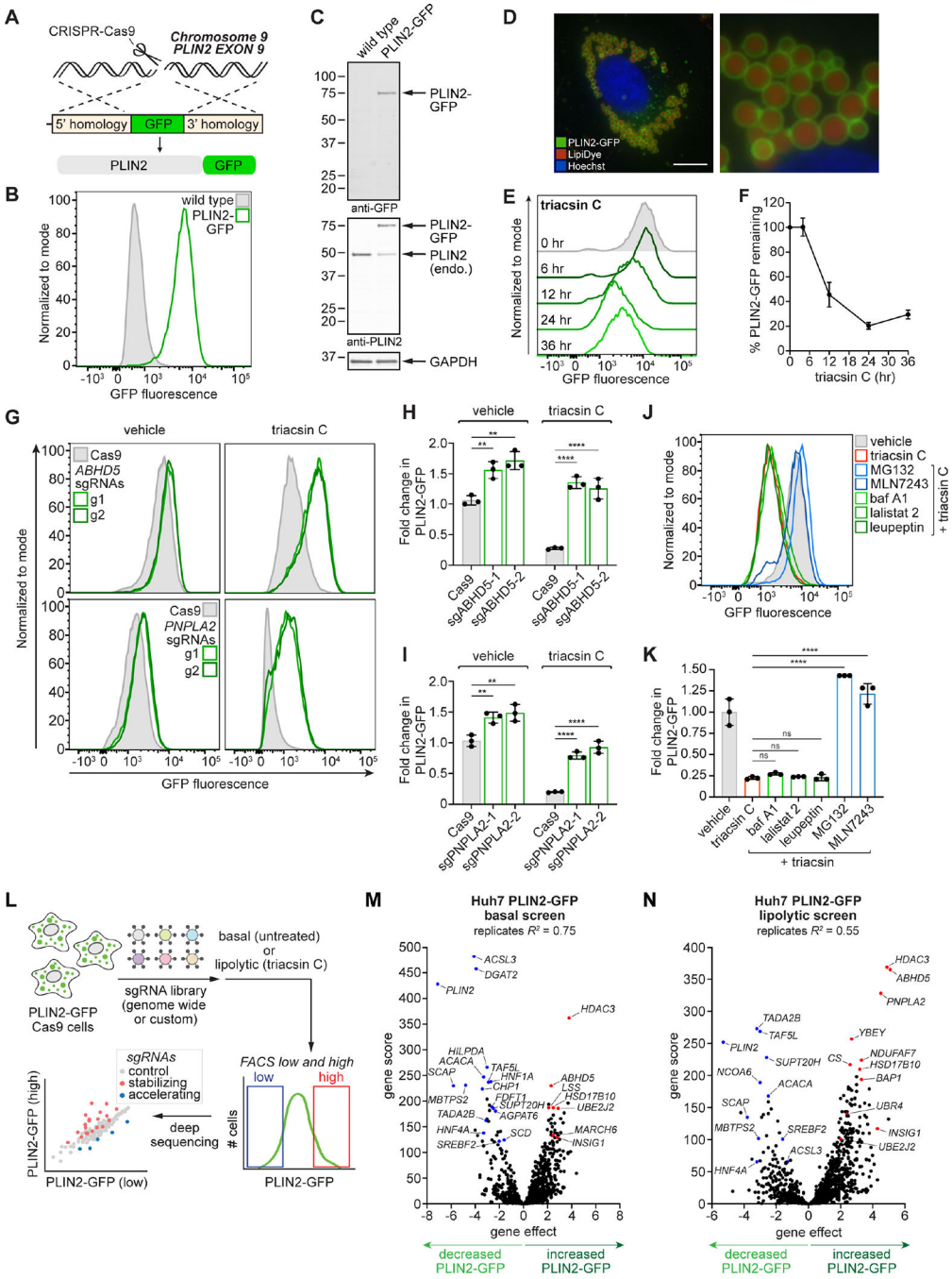

Figure 1. A genome-wide CRISPR-Cas9 screen reveals regulators of endogenously tagged PLIN2-GFP

(A) CRISPR-Cas9 strategy used to generate the PLIN2-GFP knock-in reporter cell line.

(B) Flow cytometry histogram of Huh7 parental (wild type) and PLIN2-GFP knock-in cells.

(C) Immunoblot of GFP, PLIN2, and GAPDH in parental and PLIN2-GFP Huh7 cells.

(D) Representative fluorescence microscopy image of Huh7 PLIN2-GFP cells treated with 200 μM oleate for 24 hr. LDs were stained with 500 nM Lipi-Deep Red and nuclei with 5 μg/mL Hoechst 33342. Scale bar represents 10 μm.

(E) Representative flow cytometry histograms of Huh7 PLIN2-GFP cells treated with 1 μg/ml triacsin C as indicated.

(F) Quantification of mode GFP fluorescence intensity from (E). Data represent mean ± SD of three biological replicates.

(G) Representative flow cytometry histograms of Huh7 PLIN2-GFP Cas9 expressing cells with no sgRNAs or sgRNAs against *ABHD5* (top) or *PNPLA2* (bottom). Cells were treated with 1 μg/ml triacsin C (right) or DMSO (left) for 24 hr.

(H) Quantification of the fold change in mode GFP fluorescence intensity in PLIN2-GFP Cas9 cells versus cells expressing sgRNAs against *ABHD5* from (G). Data represent mean ± SD of three biological replicates. ** $p < 0.01$, **** $p < 0.0001$ by one-way ANOVA with Dunnett's multiple comparisons test.

(I) Quantification of the fold change in mode GFP fluorescence intensity in PLIN2-GFP Cas9 cells versus cells expressing sgRNAs against *PNPLA2* from (G). Data represent mean ± SD of three biological replicates. ** $p < 0.01$, **** $p < 0.0001$ by one-way ANOVA with Dunnett's multiple comparisons test.

(J) Representative flow cytometry histogram of Huh7 PLIN2-GFP cells treated with 1 μg/ml triacsin C or 1 μg/ml triacsin C with 10 μM MLN7243, 10 μM MG132, 50 μM leupeptin, 250 nM bafilomycin A1, 10 μM lalistat 2, or DMSO for 24 hr.

(K) Quantification of fold change in mode GFP fluorescence intensity from (J). Data represent mean ± SD of three biological replicates. **** $p < 0.0001$ by one-way ANOVA with Šídák's multiple comparisons test.

(L) Schematic of FACS-based CRISPR-Cas9 screening workflow.

(M,N) Volcano plots indicating the gene effects and gene scores for individual genes from batch retest CRISPR-Cas9 screens in Huh7 PLIN2-GFP cells under basal (C) and lipolytic (D) conditions. Gene effects and gene scores were computed from two biological replicates. See also Figure S1 and S2.

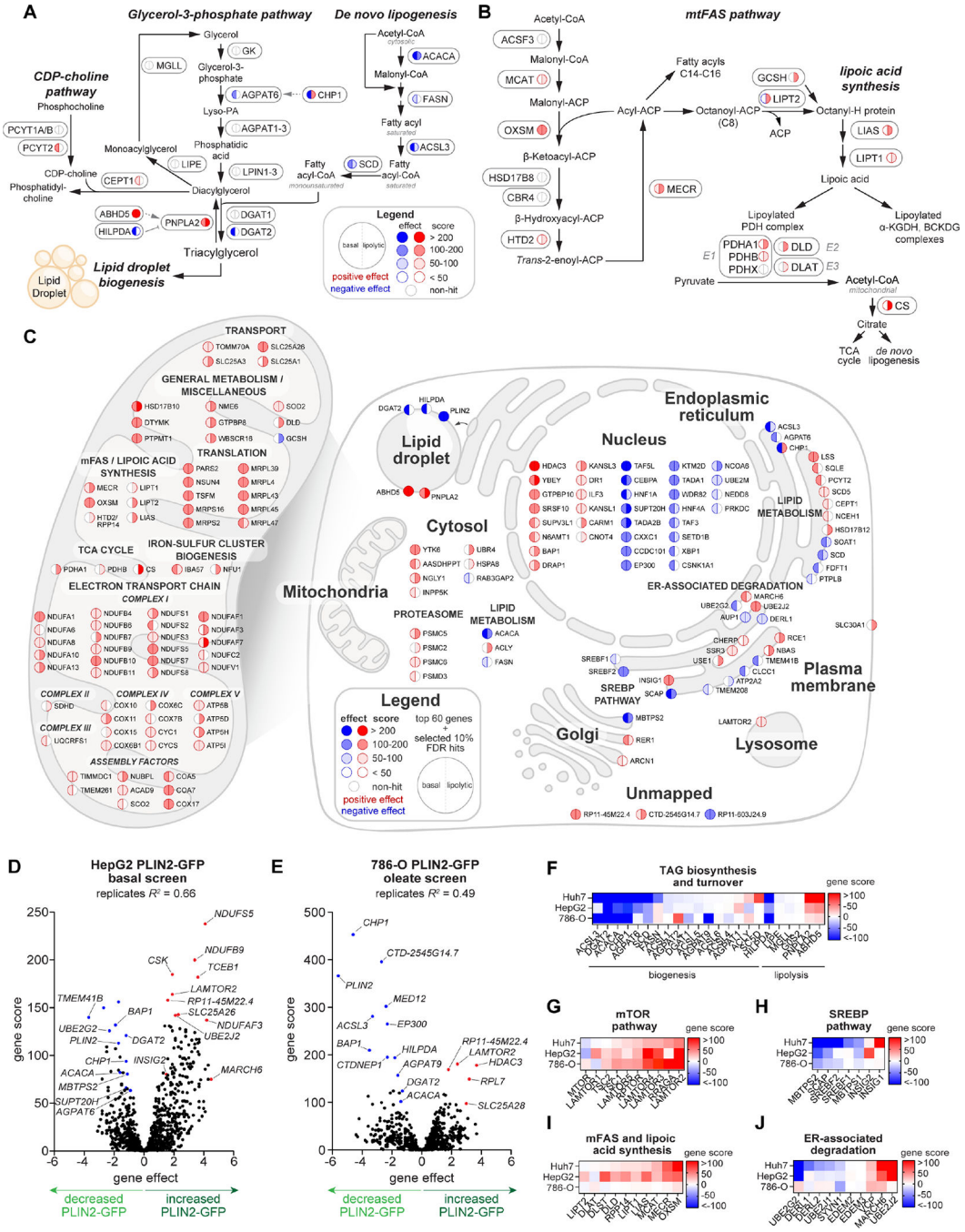

Figure 2. CRISPR-Cas9 screen identifies cell type and metabolic state-dependent regulators of PLIN2-GFP

(A,B) Schematic of the TAG synthesis and breakdown pathways (A) and the mtFAS and lipoic acid synthesis pathways as well as downstream lipoic acid-dependent pathways (B). Genes are annotated with nodes corresponding to gene effects and scores from batch retest Huh7 PLIN2-GFP basal and lipolytic screens.

(C) Cell map showing regulators of PLIN2-GFP under basal and lipolytic conditions in Huh7 cells. Map consists of the top 60 genes (ranked by gene score) from each screen

and selected genes of interest that met a 10 percent false discovery rate cutoff. Cellular localizations and functional groupings are assigned based on Gene Ontology annotations and/or previous literature.

(D,E) Volcano plots indicating the gene effects and gene scores for individual genes from CRISPR-Cas9 screens of HepG2 (D) and 786-O (E) PLIN2-GFP cells using the custom Lipid Droplet and Metabolism sgRNA Library. Gene effects and gene scores were computed from two biological replicates.

(F-J) Heat map displaying the signed gene scores TAG biosynthesis and lipolytic genes (F), mTOR genes (G), SREBP pathway-related genes (H), mtFAS and lipoic acid synthesis genes (I), and ERAD genes (J) from Huh7, HepG2, and 786-O PLIN2-GFP screens using the custom Lipid Droplet and Metabolism sgRNA Library.

See also Figure S1–S3.

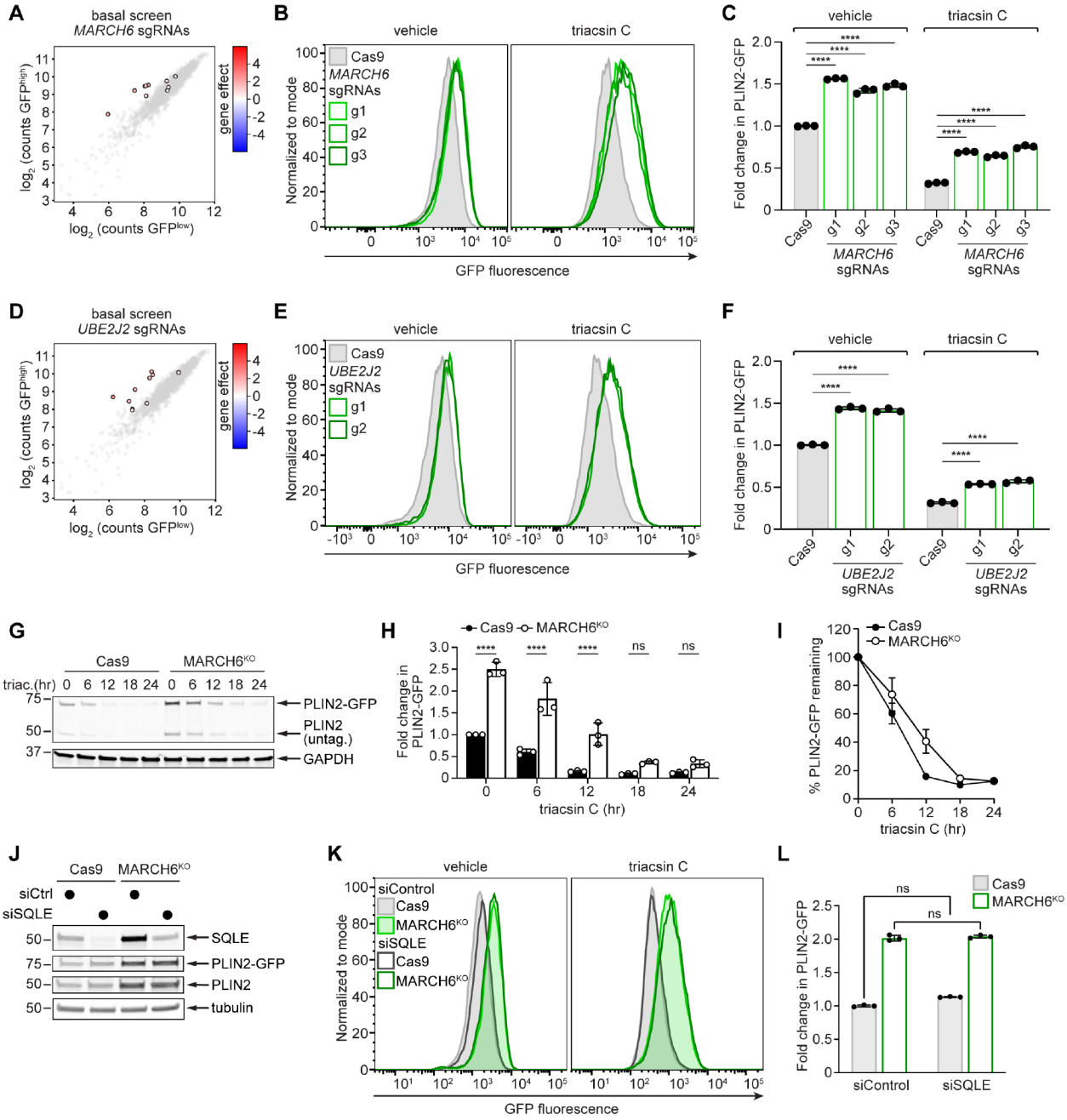

Figure 3. Regulation of PLIN2 levels by the E3 ligase MARCH6

(A) Cloud plot indicating deep sequencing counts corresponding to *MARCH6* (color scale) or negative control sgRNAs (grey scale) from one replicate of the Huh7 PLIN2-GFP basal batch retest screen from Figure 1M.

(B) Representative flow cytometry histograms of Huh7 PLIN2-GFP Cas9 cells expressing no sgRNAs or three different sgRNAs against *MARCH6* (knockout pools) following treatment with 1 μg/ml triacsin C or DMSO for 24 hr.

(C) Quantification of the fold change in mean GFP fluorescence intensity from (B). Data represent mean ± SD of three biological replicates. **** $p < 0.0001$ by one-way ANOVA with Dunnett's multiple comparisons test.

(D) Cloud plot indicating deep sequencing counts corresponding to *UBE2J2* (color scale) or negative control sgRNAs (grey scale) from one replicate of the Huh7 PLIN2-GFP basal batch retest screen from Figure 1N.

(E) Representative flow cytometry histograms of Huh7 PLIN2-GFP Cas9 cells expressing no sgRNAs or two different sgRNAs against *UBE2J2* (knockout pools) following treatment with 1 μg/ml triacsin C or DMSO for 24 hr.

(F) Quantification of the fold change in mean GFP fluorescence intensity from (E). Data represent mean ± SD of three biological replicates. **** $p < 0.0001$ by one-way ANOVA with Dunnett's multiple comparisons test.

(G) Immunoblot of PLIN2 and GAPDH in Huh7 PLIN2-GFP Cas9 and MARCH6^{KO} cells treated with 1 μg/ml triacsin C as indicated.

(H) Quantification of the fold change in PLIN2-GFP protein levels in Cas9 and MARCH6^{KO} cells from (G). Data represent mean ± SD of three biological replicates. **** $p < 0.0001$ by two-tailed, unpaired t-test.

(I) Quantification of PLIN2-GFP protein levels from (G). PLIN2-GFP protein levels were normalized to levels at time 0 hr for each cell line. Data represent mean ± SD of three biological replicates.

(J) Immunoblot of SQLE, PLIN2, and tubulin in Huh7 PLIN2-GFP Cas9 or MARCH6^{KO} cells incubated with *SQLE* or control siRNAs for 72 hr.

(K) Representative flow cytometry histograms of cells from (J). Cells were treated with 1 μg/ml triacsin C or DMSO for 24 hr.

(L) Quantification of the fold change in mean GFP fluorescence intensity in vehicle-treated cells from (K). Data represent mean ± SD of three biological replicates. No significant changes were observed by two tailed, unpaired t-test.

See also Figure S4.

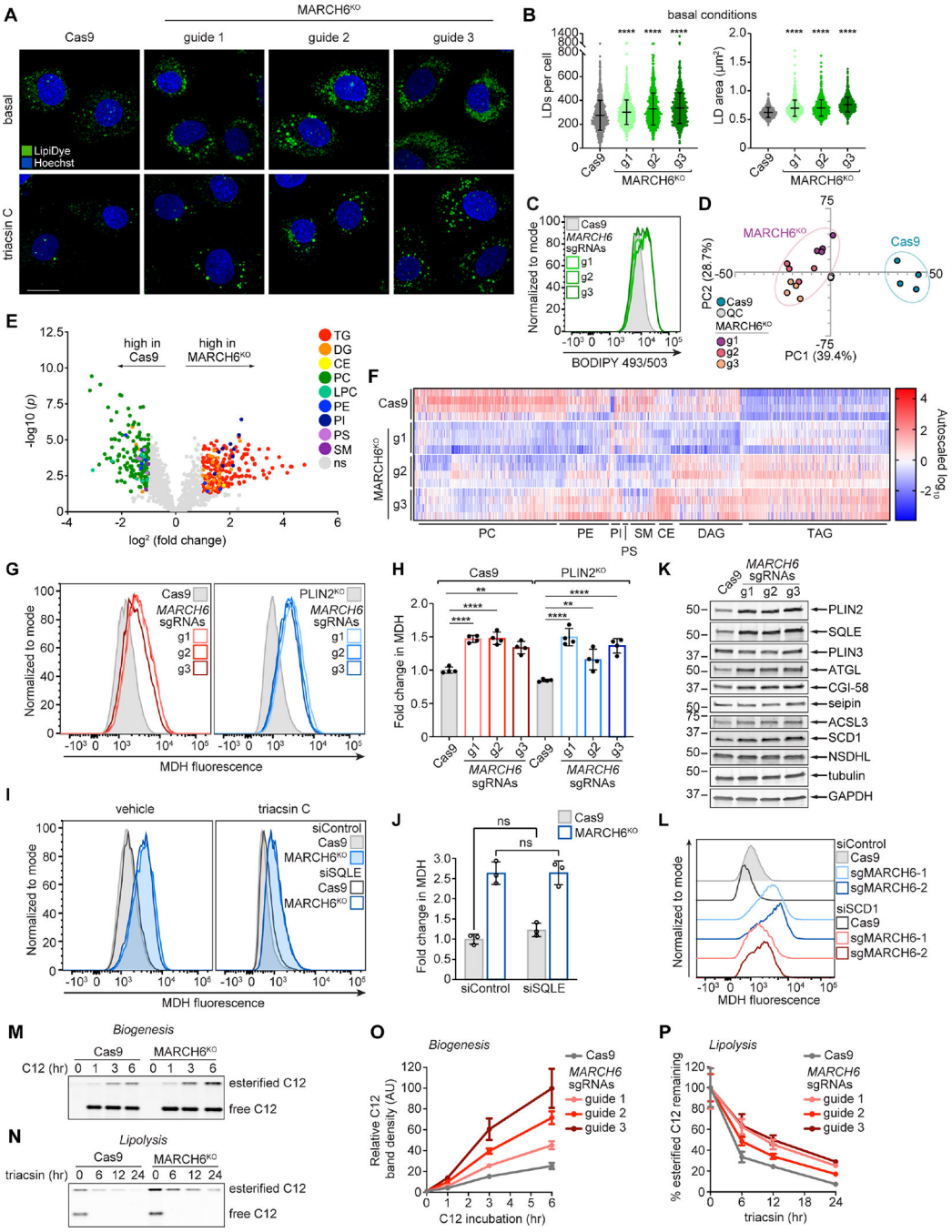

Figure 4. The E3 ligase MARCH6 regulates neutral lipid synthesis and storage independently of PLIN2

(A) Representative confocal microscopy images of Huh7 Cas9 control cells expressing a safe-targeting guide or three independent, clonally isolated MARCH6^{KO} cell lines (using three different *MARCH6* guides). Cells were imaged at the basal state or following 8 hr of treatment with 1 μg/ml triacsin C. LDs were stained with 500 nM Lipi-Green neutral lipid stain and nuclei with 5 μg/mL Hoechst 33342. Scale bar represents 20 μm.

(B) Quantification of the number (left panel) and area (right panel) of basal LDs per cell from (A). Data represent mean ± SD of three biological replicates. ****$p < 0.0001$ by one-way ANOVA with Dunnett's multiple comparisons test.

(C) Representative flow cytometry histograms of Huh7 PLIN2-GFP Cas9 cells expressing no sgRNAs or three different sgRNAs against *MARCH6*. Neutral lipids were stained with 1 μg/mL BODIPY 493/503.

(D) Principal component analysis plot (PCA) of untargeted lipidomics analysis of Huh7 Cas9 control cells expressing a safe-targeting guide or three independent, clonally isolated MARCH6^{KO} cell lines. The analysis was performed on four biological replicates.

(E) Volcano plot of untargeted lipidomics analysis of Huh7 Cas9 control cells expressing a safe-targeting guide or three independent, clonally isolated MARCH6^{KO} cell lines. The analysis was performed on four biological replicates. TG = triacylglycerol; DG = diacylglycerol; CE = cholesterol ester; PC = phosphatidylcholine; LPC = lysophosphatidylcholine; PE = phosphatidylethanolamine; PI = phosphatidylinositol; PS = phosphatidylserine; SM = sphingomyelin; ns = non-significant.

(F) Heat map indicating changes in lipid species from the untargeted lipidomics analysis of cells from (E). Data are autoscaled and normalized to the average abundance of each species presented.

(G) Representative flow cytometry histograms of Huh7 Cas9 control cells expressing a safe-targeting guide or three different sgRNAs against *MARCH6* (left panel) or Huh7 PLIN2^{KO} cells expressing a safe-targeting guide or three different sgRNAs against *MARCH6* (right panel). Neutral lipids were stained with 100 μM MDH.

(H) Quantification of the fold change in mean MDH fluorescence intensity from (G). Data represent mean ± SD of three biological replicates. ** $p < 0.01$, **** $p < 0.0001$ by one-way ANOVA with Tukey's multiple comparisons test.

(I) Representative flow cytometry histograms of Huh7 PLIN2-GFP Cas9 control and MARCH6^{KO} cells incubated with *SQLE* or control siRNAs for 72 hr and treated with 1 μg/ml triacsin C or DMSO for 24 hr. Neutral lipids were stained with 100 μM MDH.

(J) Quantification of the fold change in mean MDH fluorescence intensity in vehicle treated cells from (I). Data represent mean ± SD of three biological replicates. No significant changes were observed by two tailed, unpaired t-test.

(K) Immunoblot of the indicated proteins in Huh7 Cas9 cells expressing a safe-targeting guide or three independent sgRNAs against *MARCH6* (knockout pools).

(L) Representative flow cytometry histograms of Huh7 Cas9 cells expressing a safe-targeting guide or two independent sgRNAs against *MARCH6* (knockout pools). Cells were incubated with *SCD1* or control siRNAs for 72 hr prior to staining in 100 μM MDH.

(M) Representative thin layer chromatography (TLC) resolving esterified and free BODIPY C12 558/568 in Huh7 cells expressing a safe-targeting guide or sgRNAs against *MARCH6* (guide 2 knockout pool). Cells were incubated in BODIPY C12 for the indicated times, followed by lipid extraction and TLC.

(N) Representative TLC resolving esterified and free BODIPY C12 558/568 in Huh7 cells expressing a safe-targeting guide or sgRNAs against *MARCH6* (guide 2 knockout pool). Cells were incubated in BODIPY C12 for 16 hr followed by triacsin C treatment for the indicated times prior to lipid extraction and TLC.

(O) Quantification of esterified BODIPY C12 levels from (M). BODIPY C12 levels at each time point were quantified relative to time 0 hr for each cell line. Data represent mean ± SD of six (Cas9 cells) or three ($MARCH6^{KO}$ cells) biological replicates.

(P) Quantification of esterified BODIPY C12 levels from (N). BODIPY C12 levels at each time point were quantified relative to the 0 hr triacsin time point for each cell line. Data represent mean ± SD of six (Cas9 cells) or three ($MARCH6^{KO}$ cells) biological replicates. See also Figure S5.

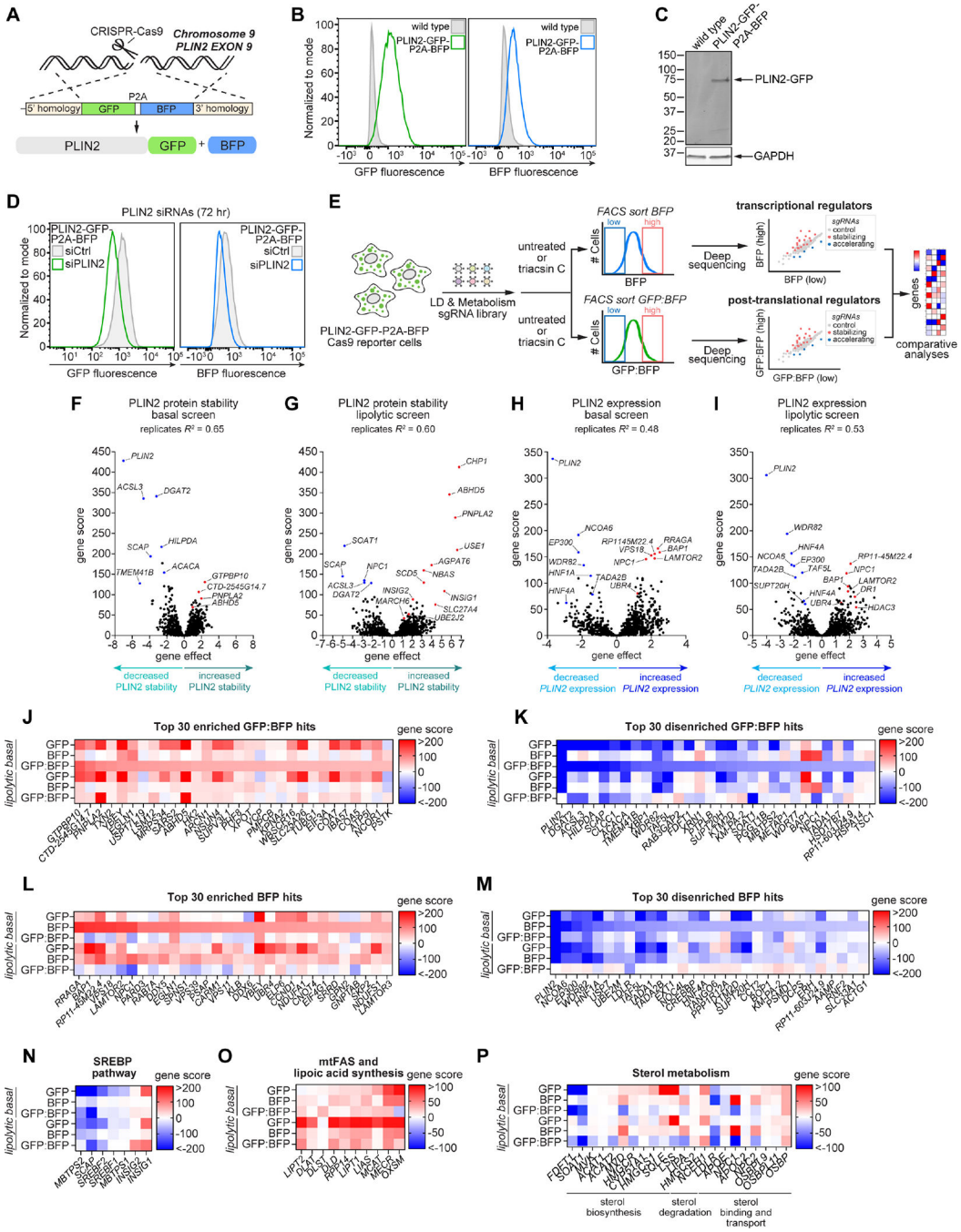

Figure 5. Analysis of pre- and post-translational PLIN2 regulators

(A) CRISPR-Cas9 strategy used to generate the PLIN2-GFP-P2A-BFP reporter cell line.

(B) Flow cytometry histograms of Huh7 parental (wild type) and PLIN2-GFP-P2A-BFP cells.

(C) Immunoblot of GFP and GAPDH in Huh7 parental and PLIN2-GFP-P2A-BFP cells.

(D) Representative flow cytometry histograms of Huh7 PLIN2-GFP-P2A-BFP cells incubated in *PLIN2* or control siRNAs for 72 hr.

(E) Schematic of batch retest CRISPR-Cas9 screens in Huh7 PLIN2-GFP-P2A-BFP cells.

(F,G) Volcano plots indicating the gene effects and gene scores for individual genes from Huh7 GFP:BFP screens under basal (F) and lipolytic (G) conditions. Gene effects and gene scores were computed from two biological replicates per screen.

(H,I) Volcano plots indicating the gene effects and gene scores for individual genes from Huh7 BFP screens under basal (H) or lipolytic (I) conditions. Gene effects and gene scores were computed from two biological replicates per screen.

(J,K) Heat maps displaying the signed gene scores of the top 30 enriched (J) and depleted (K) genes (GFP:BFP^{high} relative to GFP:BFP^{low}) from the Huh7 GFP:BFP batch retest screens under basal conditions. Signed gene scores from all other Huh7 batch retest screens are included for comparison.

(L,M) Heat maps displaying the signed gene scores of the top 30 enriched (L) and depleted (M) genes (BFP^{high} relative to BFP^{low}) from the Huh7 BFP batch retest screens under basal conditions. Signed gene scores from all other Huh7 batch retest screens are included for comparison.

(N-P) Heat maps displaying the signed gene scores of SREBP pathway-related genes (N), mtFAS and lipoic acid genes (O), and sterol metabolism-related genes (P) from batch retest GFP, BFP, and GFP:BFP Huh7 screens.

See also Figure S6.

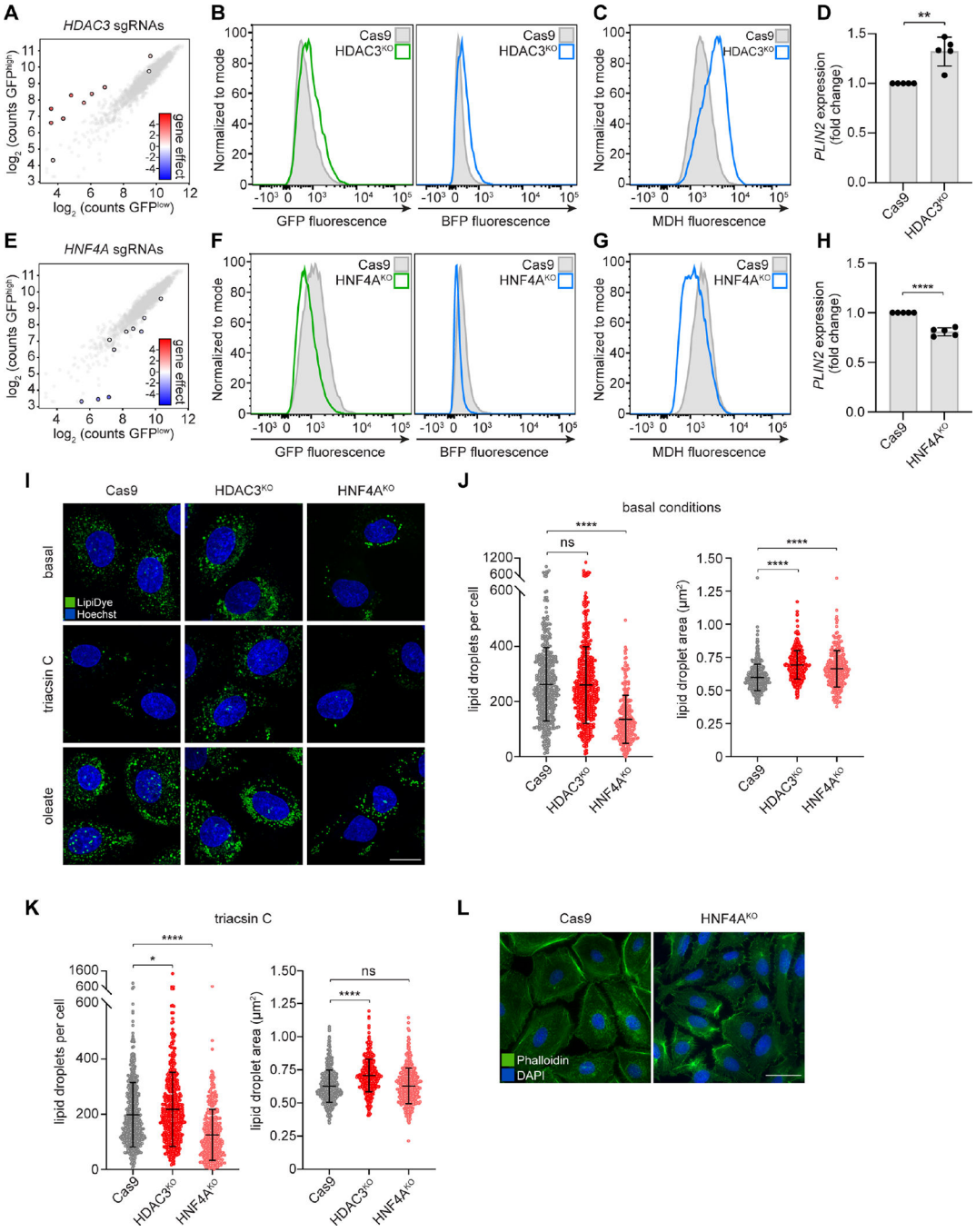

Figure 6. The transcription factor HNF4A regulates expression of PLIN2 and lipid droplet storage

(A) Cloud plot indicating deep sequencing counts corresponding to *HDAC3* (color scale) and negative control (grey) sgRNAs from one replicate of the Huh7 PLIN2-GFP batch retest screen under basal conditions.

(B) Representative flow cytometry histograms of PLIN2-GFP-P2A-BFP Cas9 cells expressing a safe-targeting guide or *HDAC3* sgRNA (knockout pool).

(C) Representative flow cytometry histograms of Huh7 Cas9 cells expressing a safe-targeting guide or *HDAC3* sgRNA (knockout pool). Neutral lipids were stained with 100 μM MDH.

(D) Relative PLIN2 mRNA levels in Huh7 Cas9 cells expressing a safe-targeting guide or *HDAC3* sgRNA, as measured by quantitative PCR. Data represent mean ± SD of five biological replicates. ** $p < 0.01$ by two tailed, unpaired t-test.

(E) Cloud plot indicating deep sequencing counts corresponding to *HNF4A* (color scale) and negative control (grey) sgRNAs from one replicate of the Huh7 PLIN2-GFP batch retest screen under basal conditions.

(F) Representative flow cytometry histograms of PLIN2-GFP-P2A-BFP Cas9 cells expressing a safe-targeting guide or *HNF4A* sgRNA (knockout pool).

(G) Representative flow cytometry histograms of Huh7 Cas9 cells expressing a safe-targeting guide or *HNF4A* sgRNA (knockout pool). Neutral lipids were stained with 100 μM MDH.

(H) Relative PLIN2 mRNA levels in Huh7 Cas9 cells expressing a safe-targeting guide or *HNF4A* sgRNA, as measured by quantitative PCR. Data represent mean ± SD of five biological replicates. **** $p < 0.0001$ by two tailed, unpaired t-test.

(I) Representative confocal microscopy images of Cas9 control cells expressing a safe-targeting guide or sgRNAs against *HDAC3* or *HNF4A*. Cells were imaged under basal conditions or following 8 hr of treatment with 1 μg/ml triacsin C or 200 μM oleate. Lipid droplets were stained with 500 nM Lipi-Green neutral lipid stain and nuclei with 5 μg/mL Hoechst 33342. Scale bar represents 20 μm.

(J) Quantification of basal LDs per cell (left panel) and LD area (right panel) from (I). Data represent mean ± SD of two biological replicates. **** $p < 0.0001$ by one-way ANOVA with Dunnett's multiple comparisons test.

(K) Quantification of LDs per cell (left panel) and LD area (right panel) following treatment with 1 μg/ml triacsin C for 8 hr from (I). Data represent mean ± SD of two biological replicates. * $p < 0.05$, **** $p < 0.0001$ by one-way ANOVA with Dunnett's multiple comparisons test.

(L) Representative fluorescence microscopy image of Huh7 Cas9 cells expressing a safe-targeting guide or sgRNAs against *HNF4A* (knockout pool). Actin was stained with Alexa Fluor 488 Phalloidin and nuclei with DAPI. Scale bar represents 50 μm.

See also Figure S7.

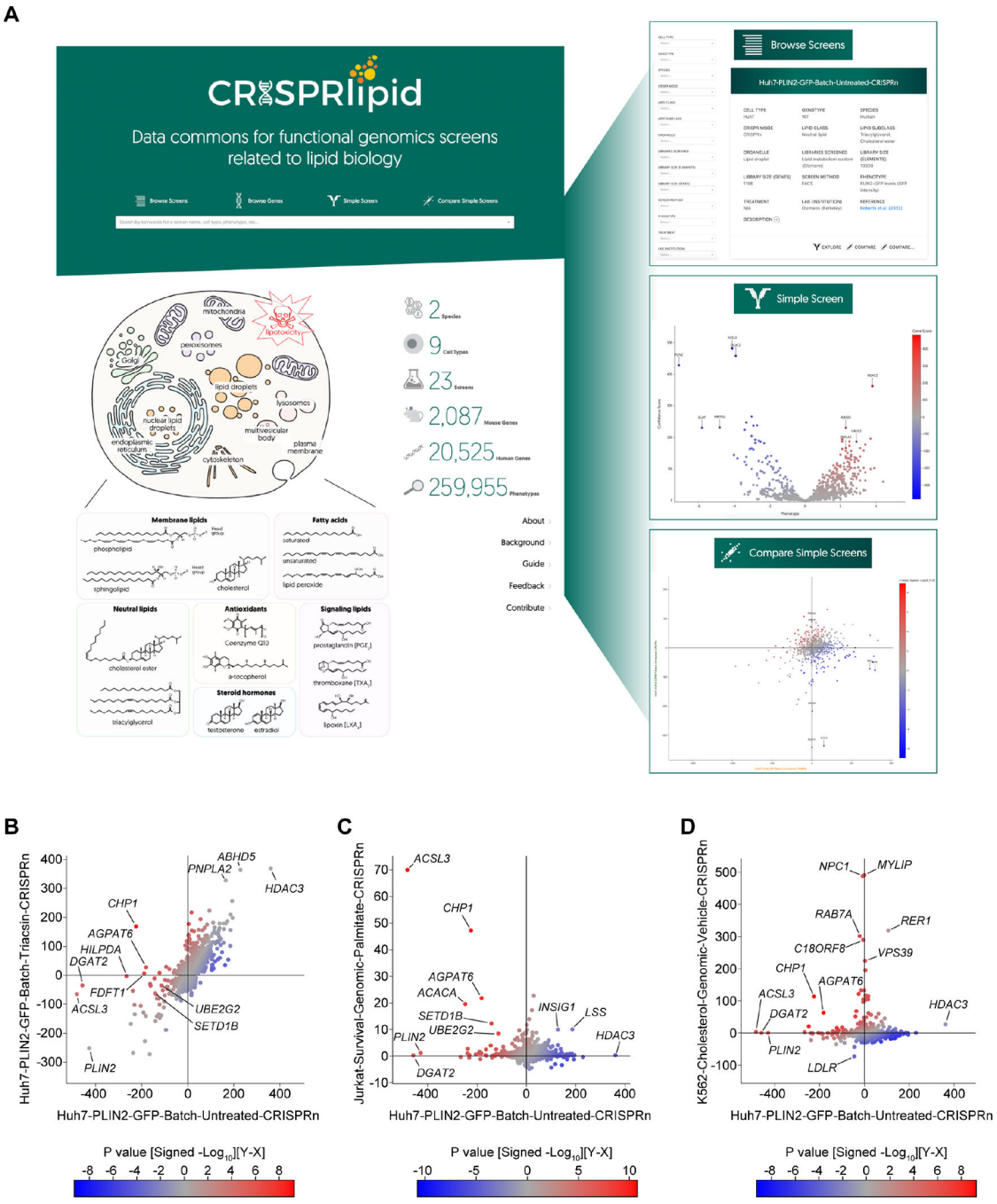

Figure 7. CRISPRlipid: A data commons for functional genomics screens related to lipid biology.

(A) Landing page for CRISPRlipid (crisprlipid.org), a data repository and tool for sharing, organizing, and analyzing functional genomics screens related to all aspects of lipid biology. Under ‘Browse Screens’ users can explore and search for CRISPR screens based on multiple parameters (e.g., cell type, lipid, organelle, and phenotype). Individual screen datasets (‘Simple Screens’) can be viewed one-by-one and explored with interactive tools, such as marking genes of interest on the plot or selecting subsets of genes that cluster together.

Under ‘Compare Simple Screens’, two screens can be plotted on one graph for comparison based on phenotypic or confidence scores.

(B-D) Scatter plot of gene scores from: (B) FACS-based PLIN2-GFP regulator screen in Huh7 cells under basal conditions (x-axis) versus lipolytic conditions (i.e., triacsin C treated, y-axis), (C) FACS-based PLIN2-GFP regulator screen in Huh7 cells (x-axis) versus palmitate survival screen in Jurkat cells (y-axis), and (D) FACS-based PLIN2-GFP regulator screen in Huh7 cells (x-axis) versus FACS-based cholesterol homeostasis screen in K562 cells (y-axis). Plots were generated using the CRISPRlipid ‘Compare Simple Screens’ tool. Color scale indicates differential p-value.

REAGENT or RESOURCE	SOURCE	IDENTIFIER
Antibodies		
Rabbit polyclonal anti-ABHD5 (CGI-58)	Proteintech	Cat#12201-1-AP; RRID:AB_2220710
Rabbit polyclonal anti-ACSL3	Invitrogen	Cat#PA5-42883; RRID:AB_2609901
Rabbit polyclonal anti-ACSL3	Invitrogen	Cat#PA5-12222; RRID:AB_2242257
Rabbit polyclonal anti-ADFP (PLIN2)	Abcepta	Cat#AP5118c; RRID:AB_10662954
Rabbit polyclonal anti-ATGL	Cell Signaling Technology	Cat#2138S; RRID:AB_2167955
Mouse monoclonal anti-ATP-citrate synthase (clone 5F8D11)	Santa Cruz Biotechnology	Cat#sc-517267
Mouse polyclonal anti-BSCL2 (seipin)	Abnova	Cat#H00026580; RRID:AB_2066666
Rabbit polyclonal anti-FABP1	Proteintech	Cat#13626-1-AP; RRID:AB_2102017
Mouse monoclonal anti-GAPDH (clone 6C5)	EMD Millipore	Cat#MAB374; RRID:AB_2107445
Mouse monoclonal anti-GFP from mouse IgG1κ (clones 7.1 and 13.1)	Roche	Cat#11814460001; RRID:AB_390913
Mouse monoclonal anti-GFP (clone B-2)	Santa Cruz Biotechnology	Cat#sc-9996; RRID:AB_627695
Mouse monoclonal anti-HDAC3 (7G6C5)	Cell Signaling Technology	Cat#3949; RRID:AB_10986336
Rabbit monoclonal anti-HNF4α (C11F12)	Cell Signaling Technology	Cat#3113; RRID:AB_2295208
Mouse monoclonal anti-NSDHL (clone D-11)	Santa Cruz Biotechnology	Cat#sc-390871
Rabbit polyclonal anti-TIP47 (PLIN3)	Proteintech	Cat#10694-1-AP; RRID:AB_2297252
Rabbit polyclonal anti-SCD1 (clone M38)	Cell Signaling Technology	Cat#2438; RRID:AB_823634
Rabbit polyclonal anti-SCD	Invitrogen	Cat#PA5-19682; RRID:AB_10982251
Mouse monoclonal anti-squalene epoxidase (clone H-6)	Santa Cruz Biotechnology	Cat#sc-271651; RRID:AB_10708249
Mouse monoclonal anti-TADA2B (clone MB-56)	Santa Cruz Biotechnology	Cat#sc-130479; RRID:AB_2201051
Rabbit polyclonal anti-α-tubulin	Abcam	Cat#ab15246; RRID:AB_301787
Rabbit polyclonal anti-UBE2J2	Proteintech	Cat#17713-1-AP; RRID:AB_2210754
Goat polyclonal anti-Rabbit IgG IRDye® 800CW Secondary Antibody	LI-COR Biosciences	Cat#926-32211; RRID:AB_621843
Goat polyclonal anti-Mouse IgG (H+L) Highly Cross-Adsorbed Secondary Antibody, Alexa Fluor™ 680	Invitrogen	Cat#A-21058; RRID:AB_2535724
Bacterial and virus strains		
Endura™ ElectroCompetent Cells	Lucigen	Cat#60242-2
NEB® 5-alpha Competent E. coli (High Efficiency)	New England Biolabs	Cat#C2987H
One Shot™ Stbl3™ Chemically Competent E. coli	Invitrogen	Cat#C737303
Chemicals, peptides, and recombinant proteins		
2,6-Di-tert-butyl-4-methylphenol, GC grade	Sigma Aldrich	Cat#B1378; CAS: 128-37-0
2-propanol, hypergrade for LC-MS	Supelco	Cat#1.02781.4000; CAS: 67-63-0
Acetonitrile, Optima® LC/MS grade	Fisher Chemical	Cat#A955-4; CAS: 75-05-8
Alexa Fluor™ 488 Phalloidin	Invitrogen	Cat#A12379
Ammonium formate, Lichropur for LC-MS	Sigma Aldrich	Cat#70221-25G-F; CAS: 540-69-2
Bafilomycin A1, *Streptomyces griseus*	Sigma Aldrich	Cat#196000; CAS: 88899-55-2

REAGENT or RESOURCE	SOURCE	IDENTIFIER
Blasticidin S HCl	Thermo Fisher Scientific	Cat#A1113903; CAS: 3513-03-9
BODIPY™ 493/503 (4,4-Difluoro-1,3,5,7,8-Pentamethyl-4-Bora-3a,4a-Diaza-s-Indacene)	Invitrogen	Cat#D3922; CAS: 121207-31-6
BODIPY™ 558/568 C12 (4,4-Difluoro-5-(2-Thienyl)-4-Bora-3a,4a-Diaza-s-Indacene-3-Dodecanoic Acid)	Invitrogen	Cat#D3835; CAS: 158757-84-7
DharmaFECT 4 Transfection Reagent	Horizon	Cat#T-2004-02
(+)-Etomoxir (sodium salt)	Cayman Chemical	Cat#11969; CAS: 828934-41-4
Formic acid, Optima® LC/MS grade	Fisher Chemical	Cat# A117-50; CAS: 64-18-6
Hexadimethrine bromide (polybrene)	Sigma Aldrich	Cat#107689; CAS: 28728-55-4
Hoechst 33342	Invitrogen	Cat#H3570; CAS: 875756-97-1
HPTLC Silica gel 60 F254 plates	Millipore Sigma	Cat#1137270001
Hygromycin B	Roche	Cat#10687010; CAS:31282-04-9
Lalistat 2	Sigma Aldrich	Cat#SML2053; CAS: 1234569-09-5
Leupeptin	Sigma Aldrich	Cat#L8511; CAS: 103476-89-7
Lipi-Blue	Dojindo Laboratories	Cat#LD01
Lipi-Green	Dojindo Laboratories	Cat#LD02
Lipi-Deep Red	Dojindo Laboratories	Cat#LD04
Methanol, HPLC grade	Fisher Scientific	Cat#A452-4; CAS: 67-56-1
MG132	Selleck Chemicals	Cat#S2619; CAS: 1211877-36-9
MLN-7243	ChemieTek	Cat#CT-M7243; CAS:1450833-55-2
Monodansylpentane (MDH)	Abcepta	Cat#SM1000b
Oleic acid	Sigma Aldrich	Cat#O1383; CAS: 112-80-1
Oligomycin-A	Selleck Chemicals	Cat#S1478; CAS: 579-13-5
Propidium iodide	Life Technologies	Cat#P3566; CAS: 25535-16-4
Puromycin Dihydrochloride	Thermo Fisher Scientific	Cat#A1113803; CAS:58-58-2
Rotenone	Sigma Aldrich	Cat#R8875; CAS: 83-79-4
SCR7	Selleck Chemicals	Cat#S7742; CAS: 14892-97-8
SPLASH ® LIPIDOMIX ® Mass Spec Standard	Avanti Polar Lipids	Cat#330707
Tert-butyl methyl ether, HPLC grade	Sigma Aldrich	Cat#34875-1L; CAS: 1634-04-4
TransIT®-293 Transfection Reagent	Mirus	Cat#2704
Triacsin C	Enzo Life Sciences	Cat#BML-EI218; CAS: 76896-80-5
Water, Optima™ LC/MS Grade, Fisher Chemical™	Fisher Chemical	Cat#W64; CAS: 7732-18-5
XtremeGENE HP DNA Transfection Reagent	Roche	Cat#6366244001
Critical commercial assays		
Herculase II Fusion Enzyme with dNTP Combo (400 rxn)	Agilent	Cat#600679
iScript RT Supermix for RT-qPCR	Bio-Rad Laboratories	Cat#1708840
QIAamp DNA Blood Mini Kit	Qiagen	Cat#51104
QIAamp DNA Blood Midi Kit	Qiagen	Cat#51183
QIAquick Gel Extraction Kit	Qiagen	Cat#28706

REAGENT or RESOURCE	SOURCE	IDENTIFIER
Qubit dsDNA HS Assay Kit	Thermo Fisher Scientific	Cat#Q32851
SsoAdvanced Universal SYBR Green Supermix	Bio-Rad Laboratories	Cat#1725271
Deposited data		
Raw and analyzed data	This paper	CRISPRlipid, http://crisprlipid.org
Experimental models: Cell lines		
Human: HEK293T cells	UC Berkeley Cell Culture Facility	N/A
Human: Hep3B cells	UC Berkeley Cell Culture Facility	N/A
Human: HepG2 cells	UC Berkeley Cell Culture Facility	N/A
Human: Huh7 cells	Kind gift from Dr. Holly Ramage (University of Pennsylvania)	N/A
Human: U-2 OS cells	UC Berkeley Cell Culture Facility	N/A
Oligonucleotides		
Table S2	N/A	N/A
Recombinant DNA		
LentiCas9-Blast	Kind gift from Dr. Feng Zhang (Massachusetts Institute of Technology)	Addgene plasmid #52962; RRID:Addgene_52962
Bassik Human CRISPR Knockout Library	Kind gift from Dr. Michael Bassik (Stanford University)	Addgene pooled libraries #101926, #101927, #101928, #101929, #101930, #101931, #101932, #101933, #101934 RRID:Addgene_101926-101934
Human Lipid Droplet and Metabolism Library	This paper	Addgene pooled library #191535; RRID:Addgene_191535
pMCB320 (puromycin resistance)	Kind gift from Dr. Michael Bassik (Stanford University)	Addgene plasmid #89359; RRID:Addgene_89359)
pMCB320 (hygromycin resistance)	This paper	N/A
pMDLg/pRRE	Addgene	Cat#12251; RRID:Addgene_12251
pRSV-Rev	Addgene	Cat#12253; RRID:Addgene_12253
pMD2.G	Addgene	Cat#12259; RRID:Addgene_12259
px330	Kind gift from Dr. Feng Zhang (Massachusetts Institute of Technology)	Addgene plasmid #42230; RRID:Addgene_42230
Software and algorithms		
Bowtie2	Langmead and Salzberg[65]	https://bowtie-bio.sourceforge.net/index.shtml; RRID:SCR_016368
CasTLE statistical framework v1.0	Morgens et al.[67]	https://github.com/elifesciences-publications/dmorgens-castle
Fiji/ImageJ	Schindelin et al.[69]	https://fiji.sc/https://imagej.net/ij/; RRID:SCR_002285
FlowJo v10	BD Biosciences	https://www.flowjo.com/solutions/flowjo; RRID:SCR_008520
Harmony High Content Image Analysis Software v4.9	Perkin Elmer	https://www.perkinelmer.com/product/harmony-4-8-office-hh17000001; RRID:SCR_018809

REAGENT or RESOURCE	SOURCE	IDENTIFIER
ICE CRISPR Analysis Tool	Synthego	https://www.synthego.com/products/bioinformatics/crispr-analysis
IE-Omics R package	Koelmel et al.[70]	http://secim.ufl.edu/secim-tools/ie-omics/
Image Lab v6.0.1	Bio-Rad Laboratories	https://www.bio-rad.com/en-us/product/image-lab-software?ID=KRE6P5E8Z
Lipostar v2.1.1	Molecular Discovery	https://www.moldiscovery.com/software/lipostar/
MetaboAnalyst 4.0	Chong et al.[72]	https://www.metaboanalyst.ca/; RRID:SCR_015539
Prism 9	GraphPad	https://www.graphpad.com/; RRID:SCR_002798
Other		
Negative control siRNA	Qiagen	Cat#1022076
ON-TARGETplus Human SCD (6319) siRNA - SMARTpool, 5 nmol	Horizon	Cat#L-005061-00-0005
ON-TARGETplus Human SQLE (6713) siRNA - SMARTpool, 5 nmol	Horizon	Cat#L-009646-00-0005